Ore Geology Reviews 72 (2016) 1–21

Contents lists available at ScienceDirect

Ore Geology Reviews

journal homepage: www.elsevier.com/locate/oregeorev

The Chapada Cu–Au deposit, Mara Rosa magmatic arc, Central Brazil: Constraints on the metallogenesis of a Neoproterozoic large porphyry-type deposit

Claudinei Gouveia de Oliveira [a,*], Frederico Bedran de Oliveira [b], Maria Emilia Schutesky Della Giustina [a], Gustavo Campos Marques [c], Elton Luis Dantas [a], Márcio Martins Pimentel [a], Bernhard Manfred Buhn [a]

[a] Universidade de Brasília, Instituto de Geociências, Brazil
[b] Ministerio das Minas e Energia, Brasília, Brazil
[c] Yamana Gold Inc., Mineração Maracá, Brazil

ARTICLE INFO

Article history:
Received 12 August 2014
Received in revised form 16 June 2015
Accepted 22 June 2015
Available online 2 July 2015

Keywords:
Goiás Magmatic Arc
Neoproterozoic
Porphyry Cu–Au deposit
Hydrothermal alteration
Kyanite-bearing rocks

ABSTRACT

The large Chapada Cu–Au deposit is situated in Goiás Magmatic Arc, Central Brazil, which is part of an accretionary orogen with tectonic evolution between ca. 900 and 600 Ma during the Brasiliano Orogeny. With a current reserve (proven and probable) of 420.94 Mt Cu (0.29%) and 479.84 Mt Au (0.25 g/t) or 3.83 Moz Au, the Chapada Cu–Au deposit is an important example of a large-tonnage, low-grade porphyry copper–gold deposit of Precambrian age, in which the mineralization is disseminated and hosted mainly by biotite-rich schists and gneisses.

In this work, we propose a two-stage genetic model for the Chapada deposit that includes an early porphyry-type Cu–Au event overprinted by a shear zone-hosted Cu–Au event. The first mineralization event represents a rare case of metamorphosed Neoproterozoic porphyry-type deposit which preserves distinct hydrothermal alteration–mineralization zoning developed at the interface between equigranular (867 ± 8 Ma) to porphyritic (884 ± 15 Ma) medium- to high-Kcalc-alkaline dioritic rocks and mafic to intermediate metavolcanic and metapyroclastic rocks. The ε_{Nd} values are positive (from +2.17 to +5.39), thus indicating the juvenile nature of the original rocks for both metavolcano-sedimentary and plutonic rocks. In this context, kyanite-rich rocks are interpreted as products of metamorphosed argillic hydrothermal alteration halo and occur as linear alignments oriented parallel to the Mara Rosa magmatic arc trend. The potassic hydrothermal alteration halo, which includes the main host rocks of the Chapada deposit, is characterized by biotite schist, muscovite–biotite schist, amphibole–biotite schist and biotite gneiss. The ore is represented predominantly by platy deformed chalcopyrite and pyrite disseminations along foliation plans (or axial surfaces of folds) and, to a lesser extent, by small massive concentrations in fold hinges. The ore shows a systematic oxide/sulfide zonation, including the peripheral pyritic shell and the central magnetite-rich zone. In general, the geological context of the deposit lacks preserved stocks, dykes and breccias, while deformed A-type quartz veins/veinlets are abundant.

The second mineralization event represents an epigenetic shear zone-hosted Cu–Au mineralization associated with D_{n+1} and occurred between 630 and 580 Ma during the late orogenic to post-orogenic stage of the Mara Rosa magmatic arc, which may be interpreted as i) a shear zone-hosted Cu–Au remobilization; ii) an orogenic Cu–Au mineralization, or iii) an intrusion-related Cu–Au mineralization. In the latter case, the mineralization could be related to the ilmenite-bearing younger metadiorite (634.8 ± 6.8 Ma) with disseminations of chalcopyrite, pyrite and pyrrhotite.

The narrow range of pyrite and chalcopyrite $\delta^{34}S$ values close to 0‰ (between −2.90 and +0.76‰) indicates that both the porphyry copper–gold mineralization and the epigenetic mineralization were generated by sulfur of magmatic origin.

1. Introduction

Porphyry-type deposits occur predominantly associated with Mesozoic to Cenozoic calc-alkaline arc rocks in the Pacific Ring of Fire, in association with oceanic lithosphere subduction (Gustafson, 1978; Mitchell and Garson, 1972; Richards, 2003; Sillitoe, 2010; Sillitoe and Perelló, 2005; Singer et al., 2008; Titley, 1993; Tosdal and Richards,

* Corresponding author at: Instituto de Geociências, Universidade de Brasília, Campus Darcy Ribeiro, 70910-900 Brasília-DF, Brazil.
E-mail address: gouveia@unb.br (C.G. Oliveira).

http://dx.doi.org/10.1016/j.oregeorev.2015.06.021
0169-1368/

2001). In addition, Hou et al. (2011) suggested that a number of significant porphyry Cu deposits in the eastern Tethyan metallogenic domain may occur in a variety of non-arc settings, from late- to post-collisional transpressional and extensional environments to intracontinental extensional environments, associated, therefore, with both orogenic and anorogenic processes. In such non-arc settings, the spatial–temporallocation of porphyries is controlled by strike-slip faults, orogeny-related transverse normal faults and lineament intersections.

Major porphyry deposits also occur within Paleozoic orogens in Central Asia and eastern North America and, to a lesser extent, within Precambrian terranes. Although Precambrian porphyry-type deposits are uncommon, important examples include: Malanjkhand, India (Sarkar et al., 1996; Sikka and Nehru, 2002; Stein et al., 2004); Boddington (2.7–2.6 Ga), Australia (Allibone et al., 1998; Duuring et al., 2007; Roth et al., 1991); Haib, Namibia (Minnit, 1986); Troilus, Quebec (Fraser, 1993); Coppin Gap, Australia (Williams and Collins, 1990); Pohjanmaa, Finland (Gaal and Isohanni, 1979); and Setting Net Lake (2.7–2.6 Ga), Canada (Ayres et al., 1982). In most cases, due to intense tectono-metamorphic overprint, the genetic signature of such deposits is not obvious. This is the case of the Boddington Au–Cu deposit, for which several genetic models have been suggested, including (i) deformed and metamorphosed syn-magmatic Archean porphyry-type deposit (Roth et al., 1991), (ii) post-peak metamorphism shear zone-hosted deposit (Allibone et al., 1998), and more recently, (iii) a two stage model including an Archean porphyry-style Cu–Au–Mo event overprinted by an intrusion-related Au–Mo event (McCuaig et al., 2001).

Porphyry-type deposits in pre-Cenozoic and especially pre-Mesozoic orogenic belts are likely to be small in size and low-grade due to their poor preservation during uplift and erosion. Conversely, large high-grade hypogene deposits usually develop in arcs built on continental crust undergoing compressive tectonics and high rates of uplift and exhumation during intrusion and mineralization (Cooke and Hollings, 2005; Kesler and Wilkinson, 2006; Richards, 2005; Seedorff et al., 2005; Sillitoe, 1997, 1998, 2008; Wilkinson and Kesler, 2009).

Hydrothermal alteration is extensive and typically zoned both at the deposit scale and also close to individual veins and fractures (Seedorff et al., 2005, 2008; Sillitoe, 2000, 2010; Titley, 1982; Tosdal et al., 2009). Typical alteration zones of porphyry-type deposits include a biotite- and/or K-feldspar-rich (± amphibole ± magnetite ± anhydrite) potassic inner zone and a quartz, chlorite, epidote, calcite propylitic outer zone with subordinate albite and pyrite. Phyllic (quartz + sericite + pyrite) and argillic alteration zones (quartz + illite + pyrite ± kaolinite ± smectite ± montmorillonite ± calcite) may occur within or between the potassic and propylitic zones or as irregular or tabular younger zones superimposed on former alteration and sulfide assemblage (Meyer and

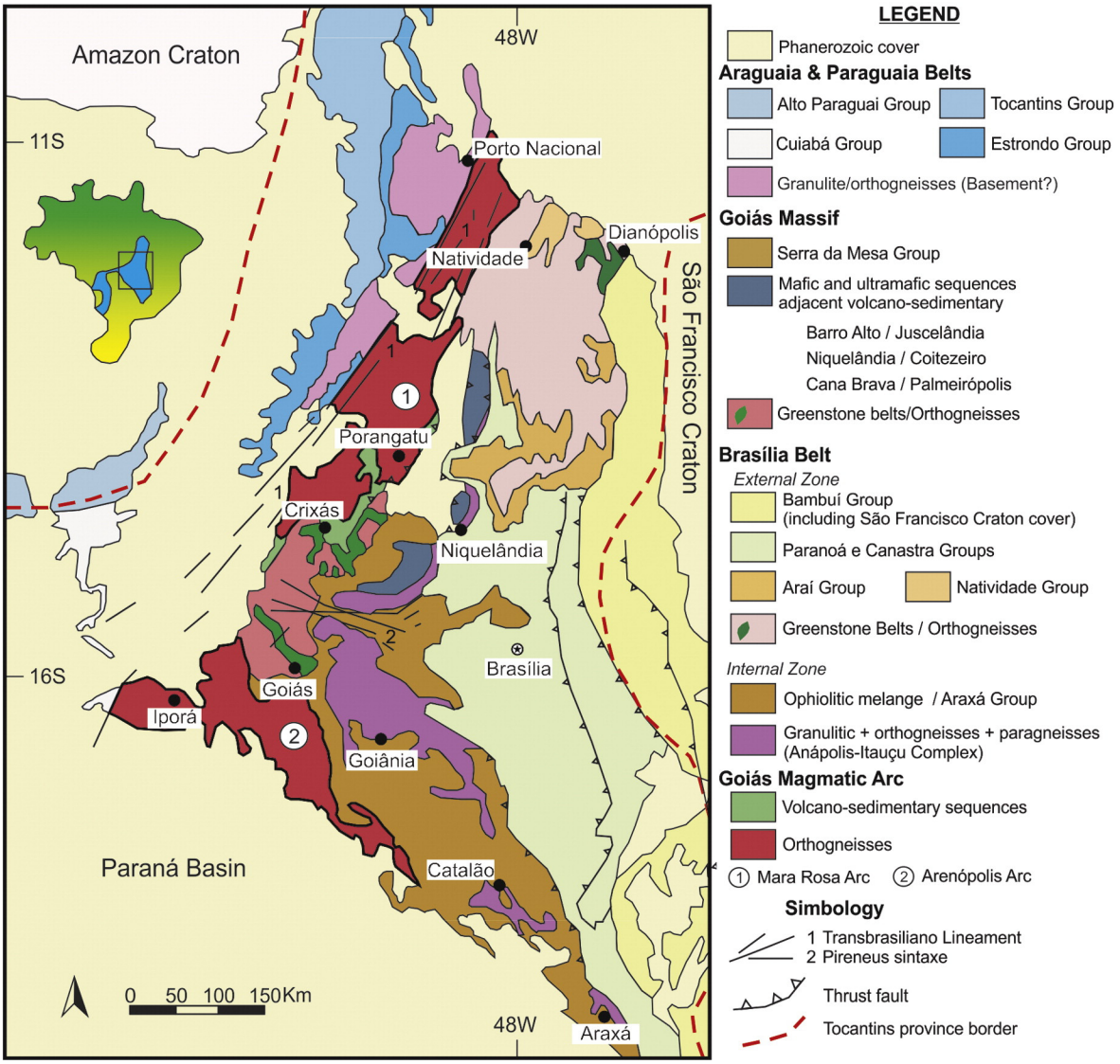

Fig. 1. Regional geologic map of the northern sector of the Tocantins Province in Central Brazil (after Fuck et al., 1994).

Hemley, 1967; Sillitoe, 2010). Economic sulfide zones are most closely associated with potassic alteration.

In this paper, we present the results of field, petrographic and isotopic studies on the Chapada Cu–Au deposit, central Brazil, identified as a porphyry-type deposit generated and metamorphosed during the Neoproterozoic Brasiliano orogeny (Oliveira et al., 2004; Richardson et al., 1986). The main goals of this study are to characterize the age and geochemical signature of the host and wall rocks of the Chapada deposit and to correlate the Cu–Au mineralization with the regional Brasiliano deformation, metamorphism and hydrothermal alteration.

2. Regional geological setting

The Goiás Magmatic Arc is located within the Brasilia Belt, Tocantins Province, formed from 900 to 600 Ma in response to oceanic lithosphere consumption, convergence and continental collision, between the Amazonian and São Francisco–Congo paleocontinents (Giustina et al., 2009; Pimentel et al., 1997), during an early phase of Gondwana supercontinent amalgamation. The tectonic zones of the belt are, from east to west (Fig. 1): a foreland zone with Archaean–Palaeoproterozoicgranite–greenstone basement covered by Neoproterozoic anchimetamorphic sedimentary rocks (Bambuí Group); a low metamorphic grade thrust-fold belt of proximal shelf successions; metamorphic nappes in upper greenschist to granulite facies of distal shelf and slope metasediments; the Goiás massif, which consists of an Archaean nucleus, comprising tonalite–trondhjemite–granodiorite (TTG) terrains and greenstone belt sequences, surrounded by the Campinorte sequence and related Palaeoproterozoic juvenile orthogneisses; and the Goiás Magmatic Arc, which represents a juvenile terrain exposed in both the northern (Mara Rosa Arc) and southern Brasilia Belt (Arenópolis Arc) (Valeriano et al., 2008).

The most evident group of structures in the Brasília Belt are extensive reverse and thrust faults system with tectonic vergence towards the São Francisco Craton, to the east (Araújo Filho, 2000; Strieder and Suita, 1999). In the northern Goiás Magmatic Arc these structures are represented by two main thrust faults: (i) the NE-trending W-dipping regional Rio dos Bois Fault, which juxtaposes Neoproterozoic magmatic arc rocks with terranes to the east and to the south including Archaean TTG terrains and greenstone belt sequences, the Paleoproterozoic Campinorte volcano-sedimentary sequence and the Neoproterozoic metasedimentary rocks of the Serra da Mesa Group; and (ii) the NNE-trending Transbrasiliano Lineament formed by dextral strike-slip shear zones. Both the Rio dos Bois and the Transbrasiliano Lineament are cut by EW,NS and NW oriented strike-slip faults that control the emplacement of large post-tectonic granitic intrusions such as the Estrela do Norte and Santa Tereza granites (Fig. 2).

3. The Goiás Magmatic Arc

The Goiás Magmatic Arc (GMA) forms a ca.1000 km NNE trending belt of Neoproterozoic juvenile orthogneisses associated with arc-typevolcano-sedimentary sequences exposed in western Goiás and

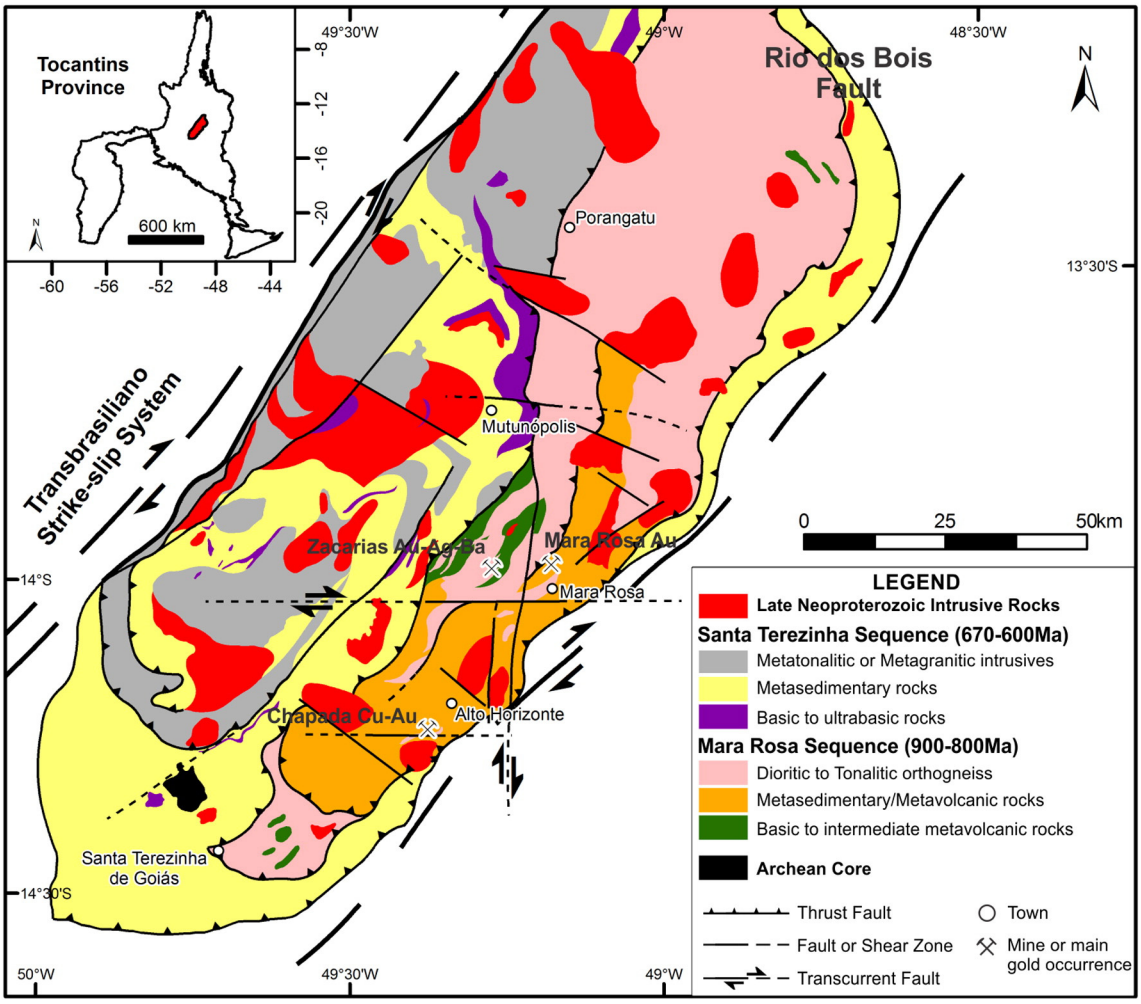

Fig. 2. Geological map of the Mara Rosa magmatic arc showing the Mara Rosa (900–800 Ma) and Santa Terezinha (670–600 Ma) metavolcano-metasedimentary sequences and the copper and/or gold deposits.

Tocantins. The southern and southern extensions of the GMA are covered by Paleozoic–Mesozoic sedimentary rocks of the Parnaíba and Paraná basins, respectively (Fig. 1).

Two discontinuous areas of Neoproterozoic juvenile continental crust form the Goiás Arc comprising dioritic to granitic orthogneisses exposed between narrow NNE anastomosed volcano-sedimentary belts: i) the northern Mara Rosa magmatic arc in which detrital metasedimentary rocks are dominant over metavolcanic and chemical metasedimentary rocks; and ii) the southern *Arenópolis Magmatic Arc* with prevalent felsic-intermediate metavolcanic rocks (Junges et al., 2002; Laux et al., 2005; Pimentel et al., 1997; Viana et al., 1995).

U–Pb zircon data indicate arc magmatism within two main periods that probably reflect distinct tectonic settings. The older event from 900 to 800 Ma took place in a setting similar to modern intra-oceanic island arcs and includes the Mara Rosa volcano-sedimentary sequence. The younger event took place from ca. 670 to 600 Ma most probably in a continental magmatic arc setting during which the Santa Terezinha volcano-sedimentary sequence formed (Fig. 2).

The Chapada Cu–Au deposit is located within the eastern belt of the Mara Rosa volcano-sedimentary sequence, which comprises three individual NW dipping narrow supracrustal belts (Arantes et al., 1991). These belts (western, central and eastern) contain metabasalt, intermediate to felsic metatuff, metaultramafic rocks, fine- to medium-grained metagraywacke, metachert, iron formation and gondite as well as a large variety of pelitic/psammitic metasedimentary and hydrothermal rocks, all metamorphosed under greenschist to amphibolite facies conditions. Small elongated syn-tectonic bodies of amphibolite (metagabbro-norite) and dioritic to granitic orthogneiss are cut by slightly deformed to completely undeformed late- to post-tectonic granite and diorite intrusions.

According to Oliveira et al. (2006), the eastern and central belts defined by Arantes et al. (1991) are part of the Mara Rosa volcano-sedimentary sequence (900 to 800 Ma) and were named metavolcano-metasedimentary sub-unit and mafic metavolcanic sub-unit, respectively. The western belt is part of the younger Santa Terezinha volcano-sedimentary sequence (670 to 600 Ma) and was named metasedimentary sub-unit (Fig. 2).

All amphibolites described in the Chapada Cu–Au deposit are characterized by low REE contents and enrichment in the LREE compared with HREE typical of island arc mafic magmas (Richardson et al., 1986). According to Kuyumjian (1989), the geochemical characteristics of the amphibolites and associated plutonic rocks of the Chapada deposit suggest an origin in a tectonic setting similar to modern volcanic arcs. On the other hand, clinopyroxene amphibolites from the same study area are more similar to those of mid-ocean ridge basalts, and therefore they may have originated in a back-arc spreading environment (Kuyumjian, 1989). To this author, it seems probable that the geological context of the Chapada Cu–Au deposit represents the remnants of a volcanic arc-back-arc basin pair. According to Pimentel et al. (1997), tonalitic to dioritic rocks have signatures similar to primitive island arc M-type granitoids and some display characteristics similar to those of modern adakites.

4. Previous studies on the Chapada Cu–Au deposit

Previous works on the Chapada deposit have highlighted controversies regarding the nature and origin of the mineralization (Oliveira et al., 2000, 2004). Richardson et al. (1986), for instance, suggested that the deposit was formed by processes similar to those observed in the genesis of porphyry-type Cu–Au deposits. On the other hand, Silva and Sá (1986) and Kuyumjian (1989) suggested a model similar to those of volcanogenic massive sulfide (VMS) deposits.

Kuyumjian (1989) arguments are based mainly on his studies on the zoning of hydrothermal alteration associated with Cu–Au mineralization. The author suggests that epidosites and epidote-rich rocks have been formed from the volcano-exhalative interaction between seawater and mafic to intermediate volcanic rocks, in a stage prior to the deformational phase D_n. The epidosites act as conduits for refluxing metal-carrier brines, including Cu and Au, while magnetite–pyrite–quartz–sericite schists could represent metamorphosed phyllic hydrothermal alteration. Kuyumjian (1989) also emphasizes the close association of staurolite- and gedrite-bearing rocks with mineralized zones, which may be indicative of metamorphosed chloritic hydrothermal alteration, while the presence of microcline schists with high contents of K_2O are suggestive of metamorphosed potassic hydrothermal alteration, which would be more strongly associated with precipitation of chalcopyrite and gold.

On the other hand, Richardson et al. (1986) used a combination of geological and geochemical features to suggest that the Chapada Cu–Au deposit shows features that resemble those described in the porphyry Cu–Au deposits formed in intra-oceanic island arc environment. According to the authors, the observed similarities include: predominance of disseminated sulfide ore; absence of massive sulfide lenses; medium to large and low-grade Cu–Au deposit; sulfides (chalcopyrite and pyrite) and oxide (magnetite) association, as well as its zoning, including pyrite-rich peripheral envelope and a magnetite-rich central core; geochemistry of hydrothermal alteration haloes indicate K_2O enriched and Na_2O and CaO depleted zones; and values of sulfur isotopic composition ($\delta^{34}S$) compatible with magmatic fluid (about 0‰).

More recently, Kuyumjian (2000, 1995) has reformulated his model approaching the model presented by Richardson et al. (1986), suggesting that the Chapada Cu–Au deposit could have been formed by a combination of processes involving magmatic epithermal hydrothermal activity, followed by metamorphic remobilization, which the author generally called the metamorphosed or modified porphyry-epithermal system.

5. The Chapada copper–gold deposit

The Chapada Cu–Au deposit is a semi-continuous body formed by the Chapada, Corpo Sul and Cava Norte orebodies that for the sake of simplification will be treated in the present study as a single body (Chapada) (Fig. 3). The Chapada orebody is characterized by disseminated chalcopyrite–pyrite largely hosted by biotite-rich schists (biotite schist, muscovite–biotite schist, amphibole–biotite schist) and subordinately by biotite gneiss, kyanite- and muscovite-rich schist and quartzite. The deposit is located in a geomorphological domain characterized by extensive plateaus covered by lateritic soils, where continuous exposures of fresh rock are rare. Open pit mining by Yamana Gold Inc. started in 2004 with final estimated open pit dimensions for the Chapada orebody of 3000 m long, 900 m wide and 220 m deep.

The main structural feature of the Chapada orebody is represented by a large open anticline, with mafic to felsic metavolcanic/metapyroclastic, metavolcanoclastic, immature metasedimentary and chemical metasedimentary rocks flanks (Fig. 4a–c), and equigranular to porphyritic metadiorite core (Fig. 4d–h). These rocks are cut by a semi-circular, weakly deformed and metamorphosed metadiorite (younger metadiorite) (Fig. 4i) and narrow N40–60°W pegmatite dykes.

The main wall rocks (unmineralized or sulfide-poor rocks) of the Chapada Cu–Au deposit are represented by magnetite–biotite gneisses and magnetite amphibolites. Magnetite–biotite gneisses are gray and show a massive to weakly foliated structure, with fine- to medium-granoblastic microstructure (Fig. 4d). It is composed mainly of plagioclase (andesine), microcline, quartz, biotite, muscovite and magnetite (±ilmenite) (Fig. 4d). Magnetite may be replaced by pyrite (pyrite–biotite gneiss), a process which is accompanied by the increase in concentration of biotite, and minor amphibole, garnet and veins/veinlets of quartz (Fig. 4d,f). In the Chapada mine, these rocks have been described as fine-grained gneisses or feldspar-bearingmeta-sandstones. However, in this work these rocks are re-interpreted as fine- to medium-grained equigranular diorite mostly metamorphosed on amphibolite facies (magnetite–biotite gneiss or equigranular

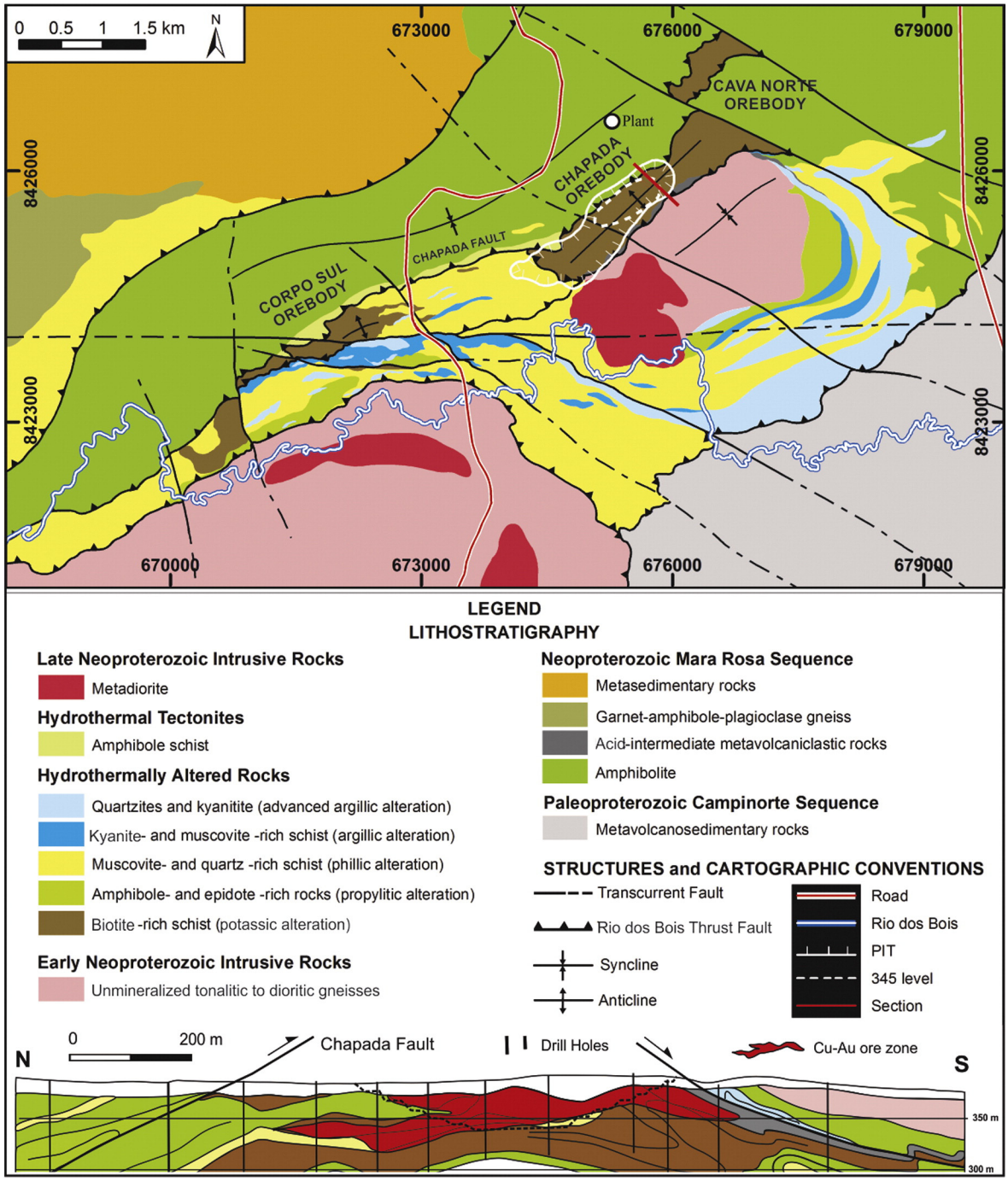

Fig. 3. Geologic map of the Chapada Cu–Au deposit including lithologic units, orebodies, major structures, and the final contour area of the open pit mine of the Chapada orebody. Dashed line indicates the 345 level detailed in the structural section of Fig. 8g.

metadiorite). In the Corpo Sul orebody, rocks with similar petrographic characteristics and chemical composition also show porphyritic texture (porphyritic metadiorite) (Fig. 4h).

Magnetite amphibolite display dark green color, diffuse foliation, fine nematoblastic microstructure and is composed mainly of amphibole, plagioclase, epidote, and minor quartz and magnetite/hematite (Fig. 4b). This rock is interpreted as basalt metamorphosed on amphibolite facies that overlie the Chapada deposit in the open pit mine (hanging wall fine-grained amphibolite or metabasalt).

The wall rocks of the Chapada deposit are cut by the semi-circular, fine-grained, weakly deformed and metamorphosed younger metadiorite, which is composed mainly of biotite, plagioclase, k-feldspar, epidote, titanite, tourmaline, besides disseminations of ilmenite/hematite, pyrite, pyrrhotite and chalcopyrite.

5.1. Host rocks

The host rocks (mineralized or sulfide-rich rocks) of the Chapada deposit include a large variety of schists, gneisses and quartzites that were grouped into five associations outlined in Fig. 3: i) amphibole- and epidote-rich rocks; ii) biotite-rich rocks; iii) muscovite and quartz-rich schist; iv) kyanite- and muscovite-rich schists; and v) quartzites and kyanitites.

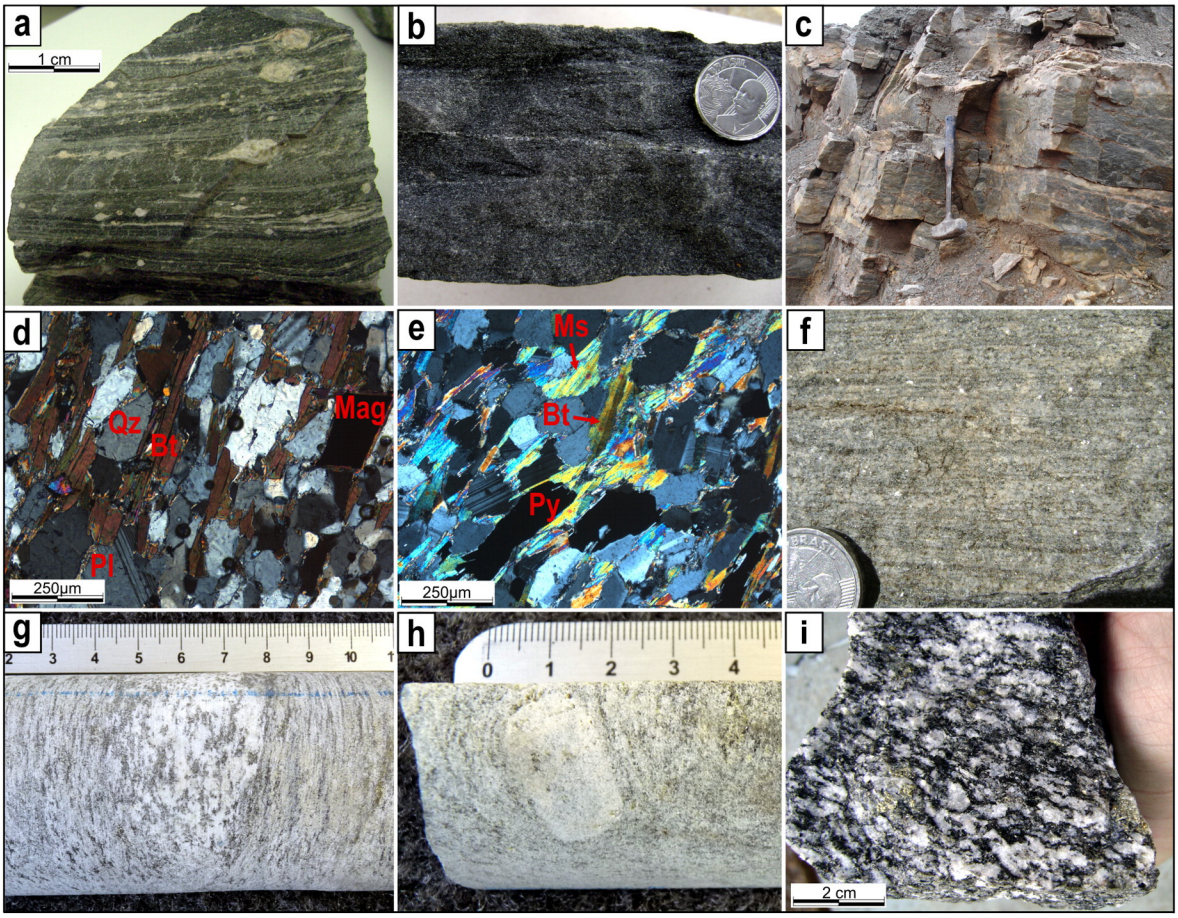

Fig. 4. Main wall rocks or texturally well-preserved rocks of the Chapada Cu–Au deposit. All samples are from open pit exposures unless otherwise noted. (a) Sample of deformed metapyroclastic rock showing sigmoidal porfiroclastic quartz–feldspar aggregates immersed on a sulfide-bearing sericitized matrix. (b) Sample of hanging-wall fine-grained amphibolite (metabasalt) consisting of amphibole, plagioclase, epidote and magnetite (±hematite, ilmenite). (c) Exposure of sulfide-bearing massive quartzite (metachert). (d and e) Thin section photomicrographies (TL, N//) of the fine-grained magnetite–biotite gneiss (equigranular metadiorite or dioritic orthogneiss) consisting of plagioclase, quartz, microcline, biotite, muscovite and magnetite (or pyrite). (f) Pyrite-bearing medium-grained biotite gneiss (equigranular metadiorite or dioritic orthogneiss). (g) Biotite gneiss showing nuclei of reliquiar, slightly deformed equigranular metadiorite. (h) Sample of porphyritic metadiorite showing pseudomorph of hydrothermalized feldspar megracryst. (i) Slightly deformed metadiorite (younger metadiorite) bearing ilmenite, pyrrhotite, pyrite and chalcopyrite. Abbreviations are: TL — transmitted light; RL — reflected light; NX — crossed nicols; and N// — parallel nicols.

Amphibole- and epidote-rich rocks association (epidosite, amphibolite, amphibole schist, epidote amphibolite and epidote gneiss) are common in the Chapada deposit as well as in its surroundings. Epidote–amphibole schists are the most important host rocks of this association. They are gray-colored to dark green, fine- to medium-grained, massive to finely foliated rocks. The foliation is defined by biotite and elongated amphibole porphyroblasts in a fine-grained granoblastic matrix formed by amphibole, epidote, biotite, quartz, plagioclase, and, minor amounts of carbonate, muscovite and chlorite. These rocks are occasionally rich in pyrite and chalcopyrite.

Biotite-rich schists and gneisses association occurs superimposed mainly on equigranular metadiorite/porphyritic metadiorite and subordinately on metavolcanic-metasedimentary sequence. It is exposed along the southern and southwestern sectors of the open pit mine and comprises a very complex petrographic association, which include biotite schist, muscovite–biotite schist, amphibole–biotite schist and biotite gneiss. These rocks are the most important host rocks of the Chapada deposit (Fig. 5a,b). Fine- to medium-grained biotite schist is the main component of this association and shows light to dark gray color and foliation defined by lepidoblastic mica-layers (biotite, ±muscovite), which envelop granoblastic quartz–feldspar domains. The mica layers can still host porphyroblasts of amphibole, kyanite, staurolite and garnet, as well as plagioclase, microcline, epidote, rutile and anhydrite. Deformed chalcopyrite, pyrite and magnetite grains occur also preferentially associated with biotite-rich domains (Fig. 5c,d).

Muscovite and quartz-rich schists association represents subordinate host rocks of the Chapada deposit, but occupies the wider area surrounding the mine (Fig. 3). These rocks are represented generically by fine- to medium-grained light gray to light green schists with well-developed schistosity and constituted mainly by muscovite, quartz, epidote and minor chlorite and biotite (Fig. 6a–c). Pyrite is the dominant sulfide, while chalcopyrite and rutile are common.

Kyanite- and muscovite-rich schist association and quartzite and kyanitite association occur as small topographic highs (Urubu ridge) in the southern and southeastern sectors of the deposit. These rocks show light-gray to light-blue color with fine- to medium-grainedmassive (quartzite and kyanitite,) to strongly foliated macrostructure (kyanite- and muscovite-rich schist) (Fig. 7a,b). In general, the schists show quartz-rich granoblastic domains enveloped by anastomosed lepidoblastic mica-layers in which kyanite appears more frequently as fine- to medium-grained elongated porphyroblasts or as medium- to coarse-grained diablastic prismatic aggregates concentrated in fold hinges. Accessory minerals include microcline, plagioclase,

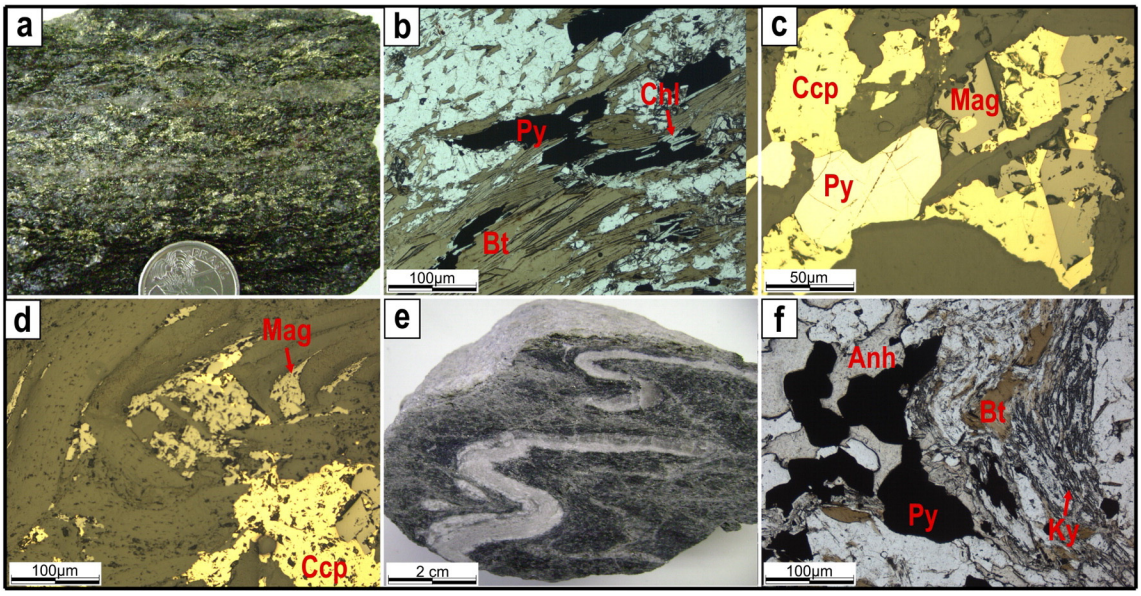

Fig. 5. Association of biotite-rich rocks. All samples are from open pit exposures unless otherwise noted. (a) Sample of chalcopyrite-rich biotite–muscovite schist showing concordant quartz veins. (b) Thin section photomicrography (TL, N//) of muscovite–biotite schist showing the relationship between sulfides and biotite. (c) Thin section photomicrography (TL, N//) of muscovite–biotite schist showing the association of chalcopyrite, pyrite and magnetite. (d) Thin section photomicrography (RL, N//) of muscovite–biotite schist showing folded and recrystallized magnetite and chalcopyrite grains. (e) Sample of sulfide-rich muscovite–biotite schist showing folded, hydrothermally altered quartz–feldsphatic vein in a matrix composed of biotite, muscovite and quartz. (f) Thin section photomicrography (TL, N//) of folded kyanite–biotite–muscovite schist showing deformed pyrite and anidrite grains. Abbreviations are: TL — transmitted light; RL — reflected light; NX — crossed nicols; and N// — parallel nicols.

epidote, staurolite, garnet, rutile, lazulite, anhydrite, roscoelite, tourmaline and corundum. These rocks are commonly pyrite-rich, chalcopyrite-poor and locally gold-rich.

5.2. Deformation and metamorphism

Structural mapping has revealed that the deformational history of the Chapada deposit took place during three main phases (D_n, D_{n+1}, D_{n+2}) related to the tectonic evolution of the Mara Rosa magmatic arc during the Neoproterozoic Brasiliano orogeny. The relationship between these deformational phases is shown in Fig. 8g.

Phase D_n produced a series of regional scale asymmetric synclines and anticlines. D_n is depicted by recumbent isoclinal (Fig. 8a) and overturned folds. This set of folds is refolded by tight coaxial asymmetrical folds that verge towards E/SE. At the open pit mine, this set of structures is well recorded in magnetite amphibolite and magnetite–biotite gneiss in which axial surfaces of NE trending isoclinal metric to decametric fold dip to NW (330–350°/10–20°) and axes plunge to N/NW (00°–10°/070°).

According to Richardson et al. (1986) and Kuyumjian (1989), peak metamorphic conditions associated with the phase D_n have been estimated at 650 °C and 9 kbar using biotite–garnet k_D thermometry, and kyanite–sillimanite, grossular–kyanite–quartz–anorthite, zoisite–kyanite–quartz–anorthite–H_2O and almandine–rutile–ilmenite–kyanite–quartz barometry. Deformation and recrystallization of sulfides (chalcopyrite and pyrite), accompanied by the growth of kyanite, sillimanite, staurolite, microcline, plagioclase, amphibole,muscovite and biotite, suggest a mineralization event prior to peak regional amphibolite facies metamorphism.

Phase D_{n+1} is related to the development of the Rio dos Bois thrust fault (or system faults), the most conspicuous structure of the Mara Rosa magmatic arc. This shear zone comprises a set of thrust to reverse faults developed in response to NNW–SSE crustal shortening. This compressive episode also produced sets of folds, mainly represented by (i) thickened hinges drag folds and asymmetry overturned parasitic folds (Fig. 8d), (ii) intrafolial folds, with hinges with quartz segregations and completely detached from limbs, (iii) isoclinal folds with boudinage along the hinge zones, and (iv) sulfide remobilization (Fig. 8b–e). Associated mylonitic foliation trends N20–50°E with moderate dips to NW (290–320°/10–40°). This foliation contains symmetric to asymmetric microlithons of gneiss and quartz segregation (Fig. 8b,c) showing a 10–30°N30–40°W (10°–30°/320°–330°) mineral stretching lineation.

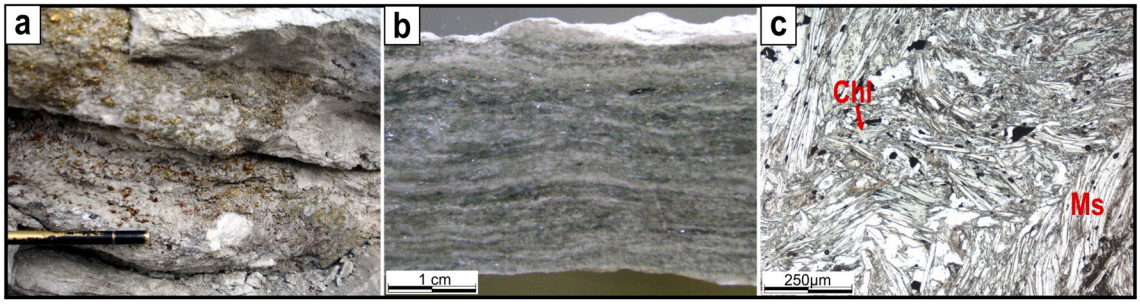

Fig. 6. Association of muscovite- and quartz-rich schists. All samples are from open pit exposures. (a) Quartz–muscovite schist outcrop showing sulfide concentration in the hinge of the recumbent isoclinal fold. (b) Chlorite–quartz–muscovite schist displaying slightly banded macrostructure highlighted by greenish chlorite-bearing bands. (c) Thin section photomicrograph (TL, N//) of the previous sample showing disseminations of rutile, pyrite and chalcopyrite in a matrix composed of muscovite, chlorite and epidote. Abbreviations are: TL — transmitted light; RL — reflected light; NX — crossed nicols; and N// — parallel nicols.

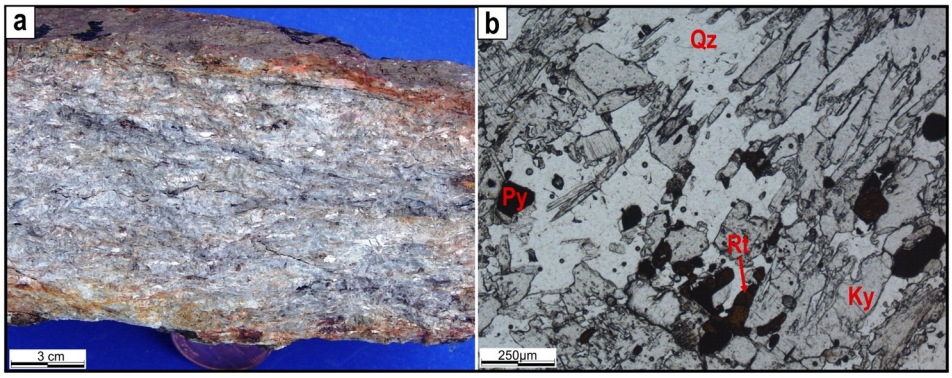

Fig. 7. Association of kyanitite and kyanite quartzite. (a) Massive kyanitite composed mainly of blue prismatic crystals of kyanite. (b) Thin section photomicrograph (TL, N//) of massive kyanite quartzite composed of granoblastic quartz, prismatic crystals of kyanite, recrystallized idioblastic pyrite and granular aggregates of rutile. Abbreviations are: TL — transmitted light; RL — reflected light; NX — crossed nicols; and N// — parallel nicols. (For interpretation of the references to color in this figure legend, the reader is referred to the web version of this article.)

This lineation, together with 00°–15°N 40–070°E (00°–15°/040°–070°) oriented fold hinges, boudin neck lines and rods indicate oblique tectonic transport towards the SE.

Kuyumjian (1989) demonstrated that the garnet rims formed during D_n amphibolite facies metamorphism re-equilibrated under greenschist facies (460 °C and 5 kbar) and ductile to brittle–ductile conditions during D_{n+1}. This process was responsible for the transformation of magnetite–biotite gneisses into muscovite–biotite schists and magnetite amphibolites into carbonate-bearing amphibole–chlorite–epidote schists.

Phase D_{n+2} includes broad open to slight asymmetric synclines (Fig. 8f) and anticlines with E–W and N–S axes that imprint a dome and keel regional pattern. This structure also controls the actual geometry of the deposit. Sets of new or existing reactivated faults and joints displace the orebody and remobilize chalcopyrite and pyrite. An outstanding north dipping E–W ductile–brittle dextral shear zone

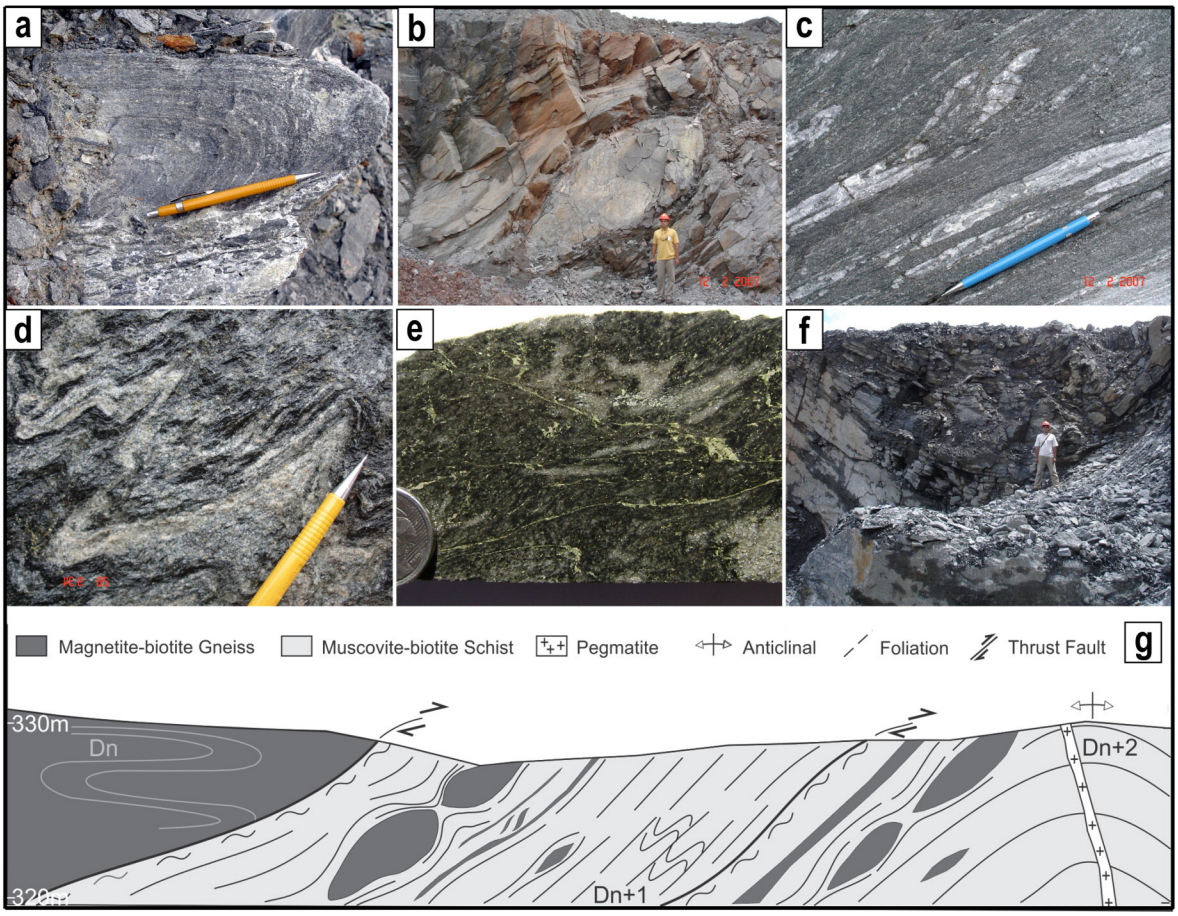

Fig. 8. Deformational structures of the Chapada deposits. All photos are from open pit exposures. (a) Isoclinal recumbent fold in fine-grained amphibolite deformed and metamorphosed during D_n. (b) Symmetric sigmoidal microlithon of fine-grained equigranular magnetite–biotite gneiss enveloped by neoformed muscovite–biotite schist during D_{n+1}. (c) Asymmetrical sigmoidal quartz segregation and tabular microlithons of fine-grained equigranular magnetite–biotite gneiss immersed in muscovite–biotite gneiss generated during D_{n+1}. (d, e) Asymmetrical tight fold developed during D_{n+1}. (f) Symmetrical open fold developed during D_{n+2}. (g) Geological and structural NW–SE cross-section through the Chapada Cu–Au deposit (indicated in Fig. 3).

reoriented the southwest part of the deposit from NE–SW to EW and truncated the orebody whose continuity beyond the shear zone to the south (Corpo Sul orebody). Sulfide remobilization (pyrite and chalcopyrite) and crystallization of idiomorphic epidote and carbonate in dilatant zones are controlled by E–W and N–S faults and sub-vertical joints whereas NW–SE trending sub-vertical faults control granitic pegmatite dyke intrusion.

Sm–Nd garnet-whole rock isochronic ages obtained from garnet-whole rock pairs of metasedimentary rocks of the Mara Rosa sequence seem to indicate an earlier amphibolite facies event at ca. 760–730 Ma, corresponding to phase D_n, and a later one of greenschist facies about 610–600 Ma relative to the phase D_{n+1} (Junges et al., 2002).

6. Analytical methods

6.1. U–Pb and Sm–Nd isotopic analyses

Zircon concentrates were extracted from ca. 10 kg rock samples using conventional gravimetric and magnetic techniques at the Geochronology Laboratory of the University of Brasília. Mineral fractions were hand-picked under a binocular microscope to obtain fractions of similar size, shape and color. For in situ U–Pb analyses, hand-pickedzircon grains were mounted in epoxy mounts and polished to obtain a smooth surface. Before analyses, mounts were cleaned with dilute (ca. 2%) HNO_3. Backscattered electron images were obtained using a FEI-QUANTA 450 working at 10 kV at the University of Brasília.

The U–Pb LA–ICPMS analyses followed the analytical procedure described by Buhn et al. (2009) and were carried out at the Geochronology Laboratory of the University of Brasília. For LA–ICPMS U–Pb analyses, samples were placed in an especially adapted laser cell. A New Wave UP213 Nd:YAG laser ($\lambda = 213$ nm), linked to a Thermo Finnigan Neptune Multi-collectorICPMS was used. Helium was used as the carrier gas and mixed with argon before entering the ICPMS. The laser was run at a frequency of 10 Hz and energy of ~100 mJ/cm^2 with a spot diameter of 30 μm.

For the U–Pb LA–ICPMS zircon analyses, a fragment of zircon standard GJ-1 (Jackson et al., 2004) was used as the primary reference material in a standard-sample bracketing method, accounting for mass bias and drift correction. The resulting correction factor for each sample analysis considers the relative position of each analysis within the sequence of 4 samples bracketed by two standard and two blank analyses (Albarède et al., 2004). An internal standard was run at the start and at the end of each analytical session, yielding accuracy around 2% and precision in the range of 1% (1σ). Uncertainties in sample analyses were propagated by quadratic addition of the external uncertainty observed for the standards to the reproducibility and within-run precision of each unknown analysis. Zircon grains with $^{206}Pb/^{204}Pb$ lower than 1000 were rejected. U–Pb age data were calculated and plotted using ISOPLOT v.3 (Ludwig, 2003) and errors for isotopic ratios are presented at the 1σ level.

Sm–Nd isotopic analyses followed the method described by Gioia and Pimentel (2000) and were carried out at the Geochronology Laboratory of the University of Brasília. Whole rock powders (ca. 50 mg) were mixed with ^{149}Sm–^{150}Nd spike solution and dissolved in Savillex capsules. Sm and Nd extractions of whole-rock samples followed conventional cation exchange techniques. Sm and Nd samples were loaded on Re evaporation filaments of double filament assemblies and the isotopic measurements were carried out on a multi-collector Finnigan MAT 262 mass spectrometer in static mode. Uncertainties for Sm/Nd and $^{143}Nd/^{144}Nd$ ratios are better than ±0.5% (2σ) and ±0.005% (2σ), respectively, based on repeated analyses of international rock standards BHVO-1 and BCR-1. The $^{143}Nd/^{144}Nd$ ratios were normalized to $^{146}Nd/^{144}Nd$ of 0.7219 and the decay constant used was 6.54×10^{-12} a^{-1}. T_{DM} values were calculated using the model of DePaolo (1981). Nd procedure blanks were better than 100 pg.

6.2. Geochemistry

Whole rock analyses were performed at Acme Analytical Laboratories Ltd., Canada. Major oxides, minor and REE elements were obtained by ICP-emission spectrometry following a lithium metaborate/tetraborate fusion and dilute nitric digestion of a sample aliquot of 0.1 g. In addition a separate 0.5 g split is digested in aqua regia and analyzed by ICPMS to report the precious and base metals. Carbon and sulfur concentrations are determined by Leco whereas loss on ignition (LOI) was measured after ignition at 1000 °C.

6.3. Mineral analyses

Mineral analyses were performed on polished thin sections using a fully automated Cameca SX-50 Electron Microprobe at the University of Brasília. Wavelength dispersive (WDS) analyses were performed at an accelerating voltage of 15 kV and a beam current of 25 nA with background counting time set to half of the peak counting time. Both synthetic and natural mineral standards were used for the analyses and the same standards and procedure reanalyzed throughout the session. Fe^{3+} contents were estimated using site and charge balance calculations on cation-normalized analyses.

6.4. Sulfur isotopic analyses

In situ sulfur isotopic analyses were carried out at the Laboratory of Geochronology of the University of Brasília, Brazil, using a Thermo Neptune multi-collector ICP–MS coupled to a 213 μm NewWave laser ablation system. A pyrite in-house standard previously calibrated against the S1 (silver sulfide), the S3 (silver sulfide) and the NBS 123 (sphalerite) international IAEA standards, was used during isotope measurements. The analyses followed a protocol similar to other previously published approaches of $^{32}S/^{34}S$ isotope determinations using a Neptune multi-collector ICP–MS (Bendall et al., 2006; Mason et al., 2006). The laser was run in raster or line mode, with a spot size of 80 μm, frequency of 10 Hz, scan speed of 2 μm per second, and energy of about 3.0 J/cm^2. Isotopes ^{32}S and ^{34}S were detected on Faraday cups with a RF generator power of 1000 W and 0.91 L/min Ar (plasma) and 0.40 L/min He (laser chamber) flux. Data reduction was done with an in-house spreadsheet which considers the blank intensity and theta (θ) values to correct for the time elapsed between the two standard and blank analyses (Albarède et al., 2004). The accuracy and the external reproducibility under these conditions are 0.3–0.4‰ (2σ), based on by multiple measurements of the S1 and S3 IAEA standards. Data are given 1σ standard deviation level, relative to the V-CDT $^{32}S/^{34}S$ value of 22.6436 (Ding et al., 2001).

7. Analytical results

7.1. Major, trace and rare earth elements lithogeochemistry

Whole-rock compositions for major, trace and REE elements of representative samples of wall rocks and host rocks of the Chapada Cu–Au deposit are shown in Table 1. Medium- to fine-grained equigranular and porphyritic metadiorites are interpreted as medium- to high-K calc-alkaline diorites (Fig. 9a–c) or calcic-alkalic to alkali-calcic diorites (Fig. 9d), most likely originated in a volcanic arc setting (Fig. 9f). Hanging wall fine-grained amphibolite (or metabasalt) consists of basalt geochemically similar to the tholeiitic basalts (Fig. 9b) or low-K calc-alkaline basalts (Fig. 9c) or calcic to calcic-alkalic basalts (Fig. 9d), typical of the early stages of development of island arc (Kuyumjian, 1989).

In general, the REE patterns of the metadiorites and one sample of the metabasalt are comparable to those observed in calc-alkaline rocks of island arcs, normally characterized by moderate light REE enrichment and by small Eu depletion (Fig. 9g). One sample of

Table 1
Representative whole-rock analyses of the Chapada Cu–Au deposit.

Rocks	Metadiorites						Muscovite–biotite Schists				Metavolcanic–metasedimentary rocks						
Sample	Chap-1	Chap-179	Chap-11	Chap-13	Cs-99	Chap-dior	Chap-2	Chap-3	Chap-4	Chap-10	Chap-6	Cn-anf	Chap-7b	Chap-1/6	Chap-8	Chap-7a	Chap-12
SiO_2	56.52	62.10	58.24	61.81	60.97	56.11	53.16	60.10	45.93	54.78	51.73	49.36	52.21	57.19	64.46	80.70	66.03
Al_2O_3	18.03	17.46	17.81	16.62	17.68	17.03	15.18	16.84	22.66	14.26	15.60	13.17	18.24	15.47	16.21	1.46	15.24
Fe_2O_3	8.92	5.50	5.97	5.52	5.02	7.55	9.83	6.50	10.62	10.59	9.25	16.21	8.28	8.02	4.70	8.99	4.28
MgO	2.95	2.54	2.32	3.41	2.21	3.87	6.57	2.75	4.52	5.79	7.40	4.92	6.21	4.75	3.75	0.11	2.42
CaO	3.91	4.07	4.85	3.46	4.03	7.03	3.65	3.70	1.53	2.23	9.36	7.8	4.80	8.87	1.53	0.10	1.73
Na_2O	3.26	3.83	4.27	2.97	3.05	3.33	1.72	3.18	1.56	2.79	1.64	2.38	2.17	1.51	2.61	0.06	2.55
K_2O	3.01	2.13	1.99	2.56	3.59	1.61	1.86	2.71	7.69	3.49	1.04	0.46	3.05	0.77	2.43	0.33	3.05
TiO_2	0.95	0.50	0.32	0.32	0.31	0.84	0.77	0.33	0.63	0.71	1.11	3.28	0.97	0.61	0.34	0.04	0.25
MnO	0.10	0.11	0.05	0.05	0.04	0.12	0.11	0.03	0.09	0.07	0.13	0.27	0.11	0.14	0.03	0.01	0.02
P_2O_5	0.36	0.16	0.22	0.26	0.23	0.22	0.31	0.22	0.24	0.27	0.62	0.58	0.29	0.21	0.20	0.07	0.19
Cr_2O_3	0.00	0.00	0.00	0.00	0	0.01	0.01	0.00	0.00	0.04	0.05	0.00	0.03	0.01	0.01	0.00	0.00
LOI	1.60	1.30	3.60	2.50	2.5	2.20	6.30	3.00	4.00	4.20	1.80	1.3	3.40	2.00	3.20	6.70	3.70
Sum	99.6	99.7	99.6	99.4	99.6	99.9	99.5	99.4	99.5	99.2	99.8	99.73	99.7	99.6	99.4	98.6	99.4
TOT/C	0.04	0.04	0.07	0.09	0.03	0.01	0.37	0.09	0.03	0.07	<0.02	<0.02	0.03	0.09	0.06	0.03	0.04
TOT/S	0.02	0.03	1.91	0.67	1.13	0.01	0.57	0.60	1.52	3.33	0.34	0.45	0.75	<0.10	0.87	6.79	1.75
Mo	0.50	0.50	155.30	2.50	3.5	<0.1	1.60	3.10	81.90	2.40	1.4	0.4	0.20	0.60	53.30	11.80	10.80
Cu	74	8	482	430	1092.5	106	2486	2357	1606	3728	104	30.5	230	74	1864	>10,000	1382
Pb	8.90	4.00	7.40	2675.40	5	0.9	80.20	7.60	6.70	6.20	14	0.7	12.50	20.30	4.60	4.10	3.00
Zn	174	60	32	51	23	52	47	32	162	91	37	26	84	71	34	29	28
Ni	2.40	6.50	5.00	3.90	5	15.2	13.60	5.00	12.40	51.90	88.7	8.7	50.40	16.50	16.90	7.60	5.00
Au*	37.30	1.20	43.80	12.30	46.5	0.9	267.10	158.40	33.80	155.50	69.2	9.3	14.90	4.40	86.40	553.80	70.80
Ag	<0.1	0.30	0.10	<0.1	0.2	<0.1	0.60	0.20	0.60	0.40	<0.1	<0.1	<0.1	<0.1	0.20	0.70	0.20
As	1.30	<0.5	2.60	<0.5	6.6	2.6	<0.5	0.60	2.40	1.50	1	1.4	<0.5	1.90	0.80	2.50	<0.5
Cd	<0.1	<0.1	<0.1	<0.1	<0.1	<0.1	2.00	<0.1	0.30	0.20	<0.1	<0.1	0.10	0.30	0.20	0.40	0.20
Tl	0.40	0.50	0.50	0.70	0.3	0.2	0.30	0.60	0.80	1.00	0.3	<0.1	0.80	<0.1	0.80	<0.1	0.40
Ba	890	692	575	652	789	389	183	515	986	404	121	185	263	212	418	44	602
Cs	0.70	0.90	1.10	1.10	1.5	3.00	1.50	1.80	1.90	3.50	0.40	0.2	1.60	0.30	0.80	<0.1	0.70
Ga	19.20	17.90	15.20	14.30	15.6	18.20	15.50	15.70	23.00	15.90	16.00	21	16.80	14.80	13.90	1.70	13.50
Hf	4.80	4.10	2.40	2.10	1.9	3.30	1.90	1.90	2.30	1.70	4.50	7	2.10	2.70	2.20	<0.1	2.30
Rb	85	83	72	84	84.3	56	61	91	190	119	35	11.2	92	26	79	7	83
Sr	478	261	744	536	593.6	528	219	564	108	219	629	267.9	205	872	297	10	284
Th	8.00	6.60	7.30	6.30	6.6	3.40	2.50	5.80	3.20	3.90	8.00	1.5	2.00	4.20	5.90	1.00	4.90
U	2.20	2.00	2.70	2.00	2	1.00	0.70	2.10	0.90	1.10	4.10	0.5	1.00	1.40	1.30	2.10	1.00
Bi	<0.1	<0.1	<0.1	1.10	<0.1	<0.1	0.50	<0.1	<0.1	<0.1	0.1	<0.1	<0.1	<0.1	<0.1	0.40	<0.1
Y	23.60	19.70	11.20	11.80	10.1	19.40	17.00	9.70	13.60	11.90	21.50	59.1	13.50	16.90	8.00	3.90	9.60
Zr	156.1	132.5	86.3	75.4	75.3	107.0	53.9	62.1	85.5	55.3	147.4	276.1	76.5	92.1	73.0	2.8	76.9
Nb	6.50	5.30	3.50	3.00	2.4	7.70	3.50	3.00	4.00	2.50	11.20	10.8	2.70	4.00	3.00	1.80	2.90
V	253	136	143	150	131	180	288	142	223	366	215	432	196	229	142	20	157
Sb	<0.1	<0.1	<0.1	<0.1	<0.1	0.2	<0.1	<0.1	<0.1	<0.1	<0.1	<0.1	<0.1	<0.1	<0.1	<0.1	<0.1
Sc	22.00	18.00	10.00	11.00	10	23	37.00	11.00	27.00	48.00	25	43	23.00	29.00	14.00	2.00	10.00
Se	0.60	<0.5	5.20	1.40	1.5	<0.5	1.50	2.90	5.10	9.00	<0.5	<0.5	1.60	0.50	4.30	24.90	4.30
La	19.20	19.30	14.70	13.10	11.9	18.80	15.00	13.90	13.30	11.10	19.80	19.3	4.30	12.50	12.10	1.10	8.90
Ce	43.10	39.60	29.50	27.10	24.7	40.00	33.10	27.70	27.80	26.00	38.90	48	11.40	29.00	23.90	2.40	19.10
Pr	5.42	4.83	3.49	3.18	2.88	4.97	4.59	3.28	3.50	3.54	4.98	6.79	1.67	3.61	2.84	0.31	2.39
Nd	23.00	19.10	13.70	12.20	11.4	20.60	21.00	13.30	15.20	17.00	20.50	33.1	8.00	15.10	11.60	1.50	9.80
Sm	4.38	3.81	2.50	2.31	2.19	4.20	4.46	2.26	2.91	3.45	4.50	9.51	2.06	3.17	2.05	0.36	1.88
Eu	1.16	0.86	0.75	0.66	0.67	1.20	1.18	0.59	0.64	0.86	1.39	3.05	0.80	0.86	0.54	0.12	0.53
Gd	4.09	3.20	2.09	2.05	1.82	3.45	3.84	1.99	2.81	3.11	4.10	11.28	2.43	3.01	1.83	0.45	1.70
Tb	0.65	0.54	0.35	0.34	0.26	0.54	0.58	0.29	0.39	0.42	0.68	1.94	0.41	0.49	0.25	0.09	0.28
Dy	3.74	3.14	1.80	1.75	1.85	3.35	3.26	1.49	2.21	2.25	4.00	11.97	2.56	2.75	1.38	0.54	1.39
Ho	0.83	0.66	0.37	0.39	0.32	0.62	0.62	0.33	0.47	0.44	0.67	2.77	0.51	0.59	0.29	0.13	0.33
Er	2.56	2.09	1.11	1.18	0.89	1.83	1.76	1.05	1.43	1.24	2.04	8.04	1.50	1.75	0.93	0.40	0.93
Tm	0.38	0.36	0.19	0.20	0.16	0.25	0.27	0.16	0.23	0.19	0.30	1.12	0.22	0.29	0.14	0.06	0.17
Yb	2.64	2.34	1.21	1.31	1.28	1.62	1.83	1.17	1.41	1.17	1.76	7.01	1.42	1.82	0.99	0.35	1.01
Lu	0.42	0.38	0.21	0.22	0.21	0.27	0.26	0.18	0.22	0.19	0.29	1.03	0.21	0.28	0.16	0.05	0.17
ΣREE	111.6	100.2	72.0	66.0	60.5	101.7	91.8	67.7	72.5	71.0	103.9	164.91	37.5	75.2	59.0	7.9	48.6

Equigranular metadiorite (magnetite–biotite gneisses): chap-1, chap-179, chap-11, chap-13; porphyritic metadiorite: cs-99; younger metadiorite: chap-dior; metabasalts: chap-6, chap-cn, chap-07b, chap-01/06; metavulcanoclastic: chap-8; and metachert: chap-07, biotite–muscovite schist: chap-12.

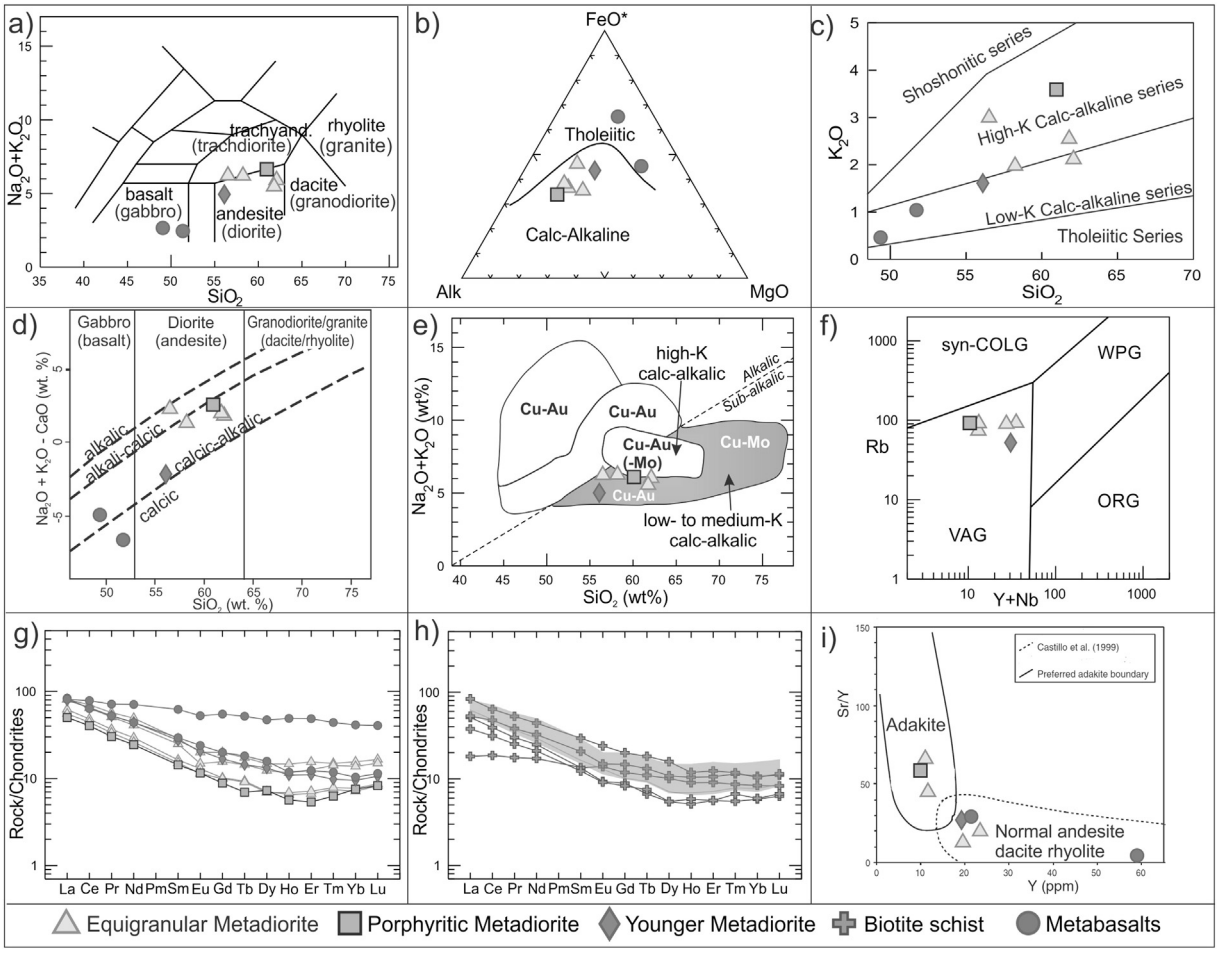

Fig. 9. (a) Plot of ($Na_2O + K_2O$) against SiO_2 diagram (TAS diagram) of Le Bas et al. (1986) adapted to classify plutonic and volcanic rocks. (b) Plots of AFM [($Na_2O + K_2O$)-FeOt-MgO] ternary diagram of Irvine and Baragar (1971) adapted to distinguish the magma series. (c) Plot of K_2O against SiO_2 diagram adapted to distinguish rock series (after Morrison, 1980). (d) Plot of ($Na_2O + K_2O - CaO$) against SiO_2 diagram of Frost et al. (2001) adapted to distinguish the rock series. (e) Plot of ($Na_2O + K_2O$) against SiO_2 diagram (TAS diagram) of Le Bas et al. (1986) adapted to classify Cu-(±Au–Mo) deposits (modified from Lang et al., 1995). (f) Log–log plot of Rb against (Y + Nb) diagram of Pearce et al. (1984) used to discriminate the tectonic settings. (g) Chondrite-normalized REE (Boynton, 1984) for metaplutonic and metavolcanic rocks. (h) Chondrite-normalized REE (Boynton, 1984) for hydrothermally altered sulfide-bearing biotite schists. The shaded area corresponds to the chondrite-normalized REE patterns for metaplutonic and metavolcanic rocks from Fig. 5f for comparison. (i) Plots of Sr/Y against Y diagram of Defant and Drummond (1993) for discriminate fields for adakite and normal island-arc andesite–dacite–rhyolite lavas. Abbreviations are: syn-COLG — syn-collision granite; ORG — orogenic granite; VAG — volcanic arc granite; and WPG — within plate granite.

metabasalt exhibits relatively flat REE pattern, with very slight enrichment in light REE, compatible with island arc tholeiite (Fig. 9g). The REE data indicate that the unaltered metadiorites and metabasalts show very similar patterns to mineralized sulfide-rich muscovite–biotite schists (Fig. 9h).

The metadioritic rocks also show geochemical signatures that transitioning between normal calc-alkaline suites and adakites, while the basaltic metavolcanics are plotted in the normal calc-alkaline field (Fig. 9i). Based on studies of porphyry and epithermal deposits (Lang et al., 1995; Richards and Kerrich, 2007), these plutonic rock types may be related to Cu–Au mineralization (Fig. 9e).

The younger metadiorite is interpreted as low-K calc-alkaline diorites (Fig. 9a–c) or calcic-alkalic diorites (Fig. 9d), most likely originated in a volcanic arc setting (Fig. 9f).

7.2. U–Pb LA–ICPMS geochronology and Sm–Nd isotopic data

7.2.1. Equigranular metadiorite (magnetite–biotite gneiss, sample Chap-FR-14)

The sample contains pink, short, and prismatic zircon grains, with well defined faces. Crystals are usually fragmented and, under BSEimaging, they show a well developed oscillatory zoning pattern. There is no evidence of zircon overgrowth or alteration due to either tectono-metamorphic or metassomatic imprint. LA–ICPMS U–Pb data obtained from sixteen grains resulted in an upper intercept age of 867 ± 8 Ma (MSWD = 1.7) (Fig. 10a, Table 2), which represents the igneous crystallization age of the protolith.

7.2.2. Porphyritic metadiorite (sample CS-99)

This sample shows centimeter-size feldspar pseudomorphs replaced by an aggregate of albite, quartz and sericite due to hydrothermal alteration. However, in spite of the pervasive fluid-related alteration evidenced by this rock, zircon grains preserve both the external and internal primary features, forming idiomorphic prismatic crystals with oscillatory zoning. There are no outer rims or any structures suggesting a recrystallization process. Eighteen U–Pb LA–ICPMS spot analyses rendered an upper intercept age of 884 ± 15 Ma (MSWD = 0.24) (Fig. 10b, Table 3), thus characterizing the age of the igneous protolith.

7.2.3. Metavolcanoclastic (feldspar–kyanite–epidote–muscovite–biotite schist, sample Chap-FR-08)

This sample, which is interpreted as a metavolcanoclastic, contains three distinct zircon populations: 1) large prismatic crystals (200–300 μm), showing the lowest values in BSE investigation; 2) stubby zircon grains (150 μm); and 3) long prisms, generally fractured and

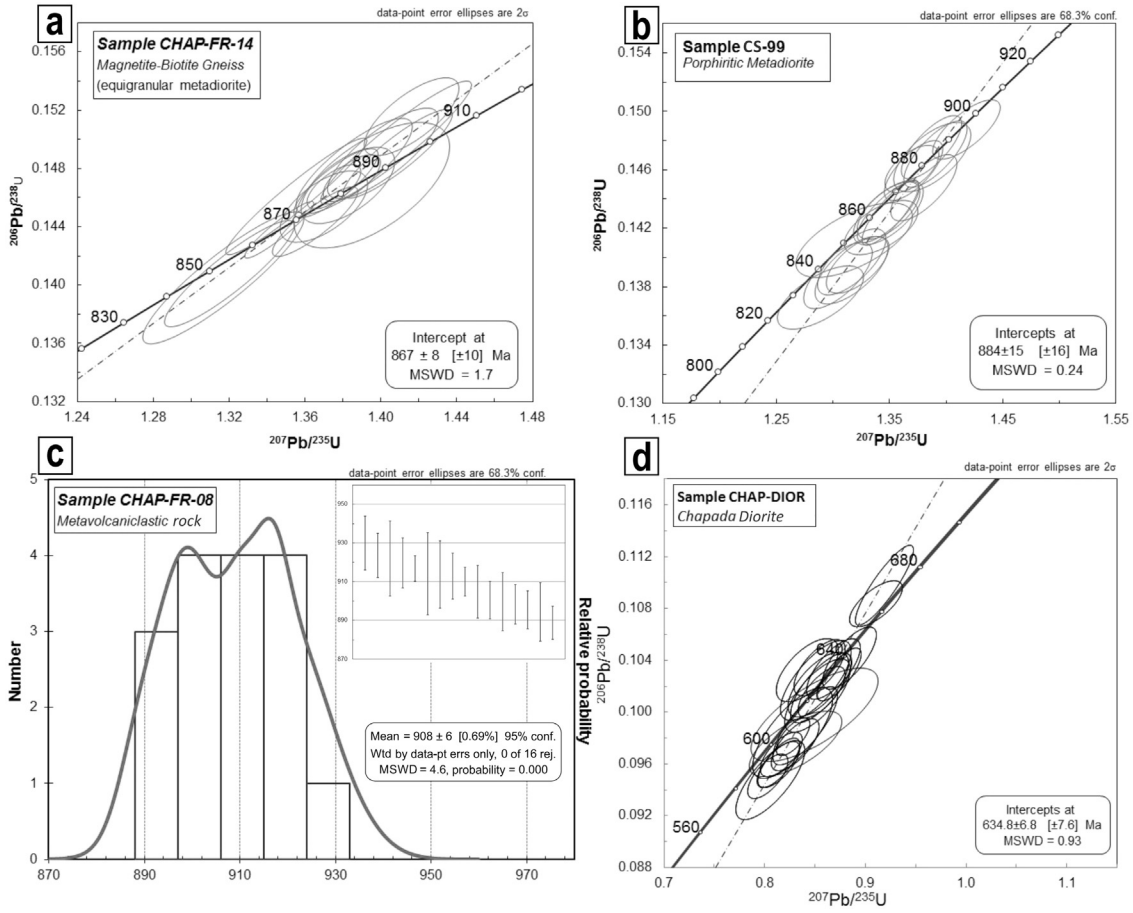

Fig. 10. (a) Weighted mean $^{206}Pb/^{238}U$ age for LA–ICP–MS analyses of zircon grains from porphyritic metadiorite of the Corpo Sul orebody. (b) Weighted mean $^{206P}b/^{238}U$ age for LA–ICP–MS analyses of zircon grains from fine-grained magnetite–biotite gneiss (equigranular metadiorite) of the Chapada orebody. (c) Probability density plot of $^{206P}b/^{238}U$ ages for LA–ICP–MS analyses of zircon grains from a metavolcanoclastic of the Chapada orebody. (d) Weighted mean $^{206P}b/^{238}U$ age for LA–ICP–MS analyses of zircon grains from younger metadiorite.

ranging in size from 100 to 200 μm. All zircon populations show little evidence of transport, and grains still preserve the subhedral to euhedral prismatic shape. Under BSE, the populations reveal a similar internal structure, with a well formed oscillatory zoning pattern. Sixteen spot analyses carried out by LA–ICPMS revealed concordant to slightly discordant ages in the interval between 930 and 890 Ma (with mean age of 908 Ma) (Fig. 10c, Table 4). Hence, this age define the timing of volcanic activity within the Mara Rosa Arc.

7.2.4. Younger metadiorite (sample Chap-Dior)

This slightly deformed metadiorite contains pink elongated prismatic zircon crystals, with well-defined faces. LA–ICPMS U–Pb data obtained

Table 2
Summary of LA–ICP–MS data for Sample CHAP-FR-14.

Sample	Isotopic ratios								Ages						
	Pb^{206}/Pb^{204}	Pb^{207}/Pb^{206}	1σ (%)	Pb^{207}/U^{235}	1σ (%)	Pb^{206}/U^{238}	1σ (%)	Rho	Pb^{207}/Pb^{206}	1σ (Ma)	Pb^{207}/U^{235}	1σ (Ma)	Pb^{206}/U^{238}	1σ (Ma)	Conc (%)
003-Z1	20,537	0.06840	0.70	1.46513	1.76	0.15537	1.76	0.97	881	14	916	11	931	15	95
005-Z3	33,143	0.06819	0.55	1.40801	1.33	0.14978	1.33	0.83	874	11	892	8	900	11	97
006-Z4	87,899	0.06858	0.46	1.40889	0.85	0.14901	0.85	0.89	886	9	893	5	895	7	99
017-Z11	19,855	0.06861	0.53	1.36536	0.79	0.14435	0.79	0.99	887	11	874	5	869	6	102
028-Z18	53,990	0.06819	0.54	1.40108	1.05	0.14904	1.05	0.59	874	11	889	6	896	9	98
030-Z20	70,491	0.06816	0.64	1.38468	0.43	0.14735	0.43	0.99	874	13	882	3	886	4	99
033-Z21	16,462	0.06830	1.26	1.38261	0.86	0.14684	0.86	0.62	878	26	882	5	883	7	99
035-Z23	20,160	0.06892	1.43	1.39529	1.07	0.14685	1.07	1.00	896	29	887	6	883	9	101
048-Z32	94,407	0.06730	0.56	1.35547	1.29	0.14609	1.29	0.79	847	12	870	8	879	11	96
057-Z37	288,488	0.06797	0.61	1.37524	0.55	0.14676	0.55	0.95	868	13	878	3	883	5	98
058-Z38	18,980	0.06835	1.14	1.36995	0.73	0.14539	0.73	0.62	879	23	876	4	875	6	100
059-Z39	256,962	0.06802	0.73	1.32020	1.47	0.14078	1.47	0.91	869	15	855	8	849	12	102
060-Z40	36,380	0.06792	0.42	1.34643	0.85	0.14380	0.85	0.93	866	9	866	5	866	7	100
064-Z42	62,860	0.06799	0.97	1.31700	1.79	0.14050	1.79	0.99	868	20	853	10	847	14	102
066-Z44	32,856	0.06791	0.47	1.37633	0.88	0.14700	0.88	0.95	866	10	879	5	884	7	98
070-Z46	27,395	0.06778	1.04	1.41618	0.72	0.15156	0.72	0.72	862	21	896	4	910	6	95
072-Z48	309,444	0.06785	0.76	1.38594	1.19	0.14817	1.19	0.63	864	16	883	7	891	10	97

Table 3
Summary of LA–ICP–MS data for Sample CS-99.

Sample	Isotopic ratios								Ages						
	Pb^{206}/Pb^{204}	Pb^{207}/Pb^{206}	1σ (%)	Pb^{207}/U^{235}	1σ (%)	Pb^{206}/U^{238}	1σ (%)	Rho	Pb^{207}/Pb^{206}	1σ (Ma)	Pb^{207}/U^{235}	1σ (Ma)	Pb^{206}/U^{238}	1σ (Ma)	Conc (%)
004-z1	128,177	0.06813	0.8	1.3712	1.2	0.14596	0.9	0.73	872.6	17.2	876.7	7.3	878.3	7.6	101
006-z3	154,442	0.06913	1.1	1.4179	1.4	0.14876	0.9	0.74	902.6	21.8	896.5	8.3	894.0	7.5	99
007-z4N	72,188	0.06847	0.7	1.3507	1.2	0.14308	1.0	0.83	882.8	13.6	867.9	7.1	862.0	8.3	98
009-z5N	73,077	0.06818	1.1	1.3044	1.5	0.13877	1.1	0.69	873.9	22.6	847.7	8.8	837.7	8.5	96
010-z5B	216,713	0.06835	0.9	1.3488	1.3	0.14311	1.0	0.78	879.3	19.2	867.0	7.8	862.2	7.8	98
015-z8	126,397	0.06818	0.8	1.3870	1.3	0.14755	1.0	0.75	874.0	16.9	883.4	7.5	887.2	8.1	102
017-z10	125,733	0.06915	0.9	1.3803	1.4	0.14477	1.0	0.72	903.2	19.4	880.6	8.2	871.6	8.4	96
018-z11	134,353	0.06857	0.8	1.3906	1.3	0.14708	1.0	0.75	885.9	17.5	884.9	7.8	884.6	8.4	100
024-z14	177,028	0.06802	0.9	1.3698	1.1	0.14606	0.7	0.60	869.0	18.3	876.1	6.7	878.8	6.0	101
025-z15	83,215	0.06832	1.0	1.3491	1.4	0.14321	0.9	0.64	878.4	21.0	867.2	7.9	862.8	7.3	98
026-z16	70,049	0.06811	1.6	1.2889	1.9	0.13726	1.0	0.65	871.8	34.1	840.8	11.1	829.2	8.1	95
027-z17	99,819	0.06835	1.1	1.3166	1.5	0.13970	1.1	0.69	879.3	22.1	853.0	8.7	843.0	8.5	96
030-z20	71,454	0.06775	2.3	1.3188	2.6	0.14119	1.2	0.63	860.8	47.4	854.0	14.9	851.4	9.5	99
033-z21	181,502	0.06853	1.2	1.3877	1.6	0.14687	1.1	0.64	884.5	25.2	883.7	9.6	883.4	8.8	100
034-z22	82,143	0.06838	1.1	1.3490	1.5	0.14307	1.0	0.65	880.2	23.1	867.1	8.8	862.0	8.2	98
035-z23	261,131	0.06872	1.0	1.3218	1.4	0.13950	0.9	0.64	890.4	21.3	855.3	8.0	841.8	7.3	95
036-z24	215,744	0.06854	1.3	1.3425	1.6	0.14205	0.9	0.60	885.0	27.9	864.3	9.3	856.2	6.9	97
039-z27	115,972	0.06862	1.2	1.3164	1.6	0.13913	1.1	0.66	887.4	24.6	852.9	9.4	839.8	8.7	95

from eighteen grains resulted in an upper intercept age of 634.8 ± 6.8 Ma (MSWD = 0.9) (Fig. 10d, Table 5), which is interpreted as representative of the igneous crystallization age.

7.3. Whole-rock Sm–Nd analyses

Samples representing both the wall rocks and host rocks of the Chapada ore deposit were selected for the Sm–Nd isotope investigation (Table 6). $^{147}Sm/^{144}Nd$ values vary from 0.115 to 0.169, and T_{DM} model ages are between 0.9 and 1.2 Ga. The ε_{Nd} values are positive and range from +2.17 to +5.39, thus indicating the juvenile nature of the original rocks of the Chapada deposit (Fig. 11).

8. The Chapada Cu–Au mineralization

In this work, we conclude that the Chapada Cu–Au mineralization is more complex and also more diverse than summarized in Section 4. The deposit was formed by a combination of processes involving a first event of syngenetic Cu–Au mineralization, similar to the porphyry systems as discussed by Richardson et al. (1986), followed by a second event of epigenetic shear zone Cu–Au mineralization formed during D_{n+1}.

8.1. Porphyry-type Cu–Au mineralization

In the Chapada Cu–Au deposit, as well as in other Cu–Au deposits and occurrences of the Mara Rosa magmatic arc (Serra das Araras, Serra dos Picos, Serra do Caranã and Serra do Bom Jesus) and Au (Posse, Zacarias) the occurrence of kyanite-rich rocks is common (Fig. 15). These rocks appear frequently as blocks and boulders along the slopes of narrow and linear ridges. Other kyanite-bearing rocks, represented by kyanite quartzite, muscovite–kyanite quartzite, muscovite–kyanite–quartz schist, kyanite–garnet–muscovite schist, kyanite–biotite–muscovite and quartz–plagioclase–kyanite–muscovite schist, occur as lenses or irregular bodies with varied dimensions. In general, these rocks contain rutile as a frequent accessory mineral, in addition to corundum, lazulite, anhydrite, roscoelita (V-muscovite), tourmaline and, sporadically, gold. Pyrite is the dominant sulfide, sometimes in high modal concentrations (>10%), whereas chalcopyrite is subordinate, or more commonly, absent. Kyanite often occurs as prismatic syn-kinematic porphyroblasts, and to a lesser extent, as diablastic tabular porphyroblasts, concentrated in fold hinges. In the 1980s, the kyanite-rich rocks of the Serra das Araras were mined and its concentrate was used in the refractory industry.

The kyanite-rich rocks of the Chapada deposit occur in association with dioritic (equigranular metadiorite, porphyritic metadiorite) and

Table 4
Summary of LA–ICP–MS data for sample CHAP-FR-08.

Sample	Isotopic ratios								Ages						
	Pb^{206}/Pb^{204}	Pb^{207}/Pb^{206}	1σ (%)	Pb^{207}/U^{235}	1σ (%)	Pb^{206}/U^{238}	1σ (%)	Rho	Pb^{207}/Pb^{206}	1σ (Ma)	Pb^{207}/U^{235}	1σ (Ma)	Pb^{206}/U^{238}	1σ (Ma)	Conc (%)
003-Z1	130,385	0.06786	0.57	1.39254	0.84	0.14885	0.84	0.89	864	12	886	5	894	7	97
005-Z3	49,930	0.06894	0.47	1.42139	0.74	0.14954	0.74	0.84	897	10	898	4	898	6	100
006-Z4	45,326	0.06730	0.97	1.39101	0.64	0.14992	0.64	0.64	847	20	885	4	900	5	94
009-Z5	103,365	0.06831	0.48	1.41035	1.12	0.14976	1.12	0.94	878	10	893	7	900	9	98
010-Z7	48,674	0.06817	0.41	1.40057	0.69	0.14902	0.69	0.87	874	8	889	4	895	6	98
011-Z8	13,808	0.06775	0.31	1.42111	0.80	0.15214	0.80	0.91	861	7	898	5	913	7	94
015-Z9	131,424	0.06761	0.27	1.41948	1.77	0.15228	1.77	0.99	857	6	897	10	914	15	94
016-Z10	47,255	0.06765	0.45	1.44725	0.89	0.15518	0.89	0.93	858	9	909	5	930	8	92
017-Z11	51,824	0.06766	0.53	1.41428	0.49	0.15162	0.49	0.66	858	11	895	3	910	4	94
022-Z14	16,235	0.06833	0.41	1.45111	0.70	0.15404	0.70	0.92	879	9	910	4	924	6	95
023-Z15	15,411	0.06874	0.51	1.44851	0.51	0.15285	0.51	0.63	891	11	909	3	917	4	97
024-Z16	12,418	0.06842	0.80	1.39449	0.65	0.14783	0.65	0.76	881	16	887	4	889	5	99
027-Z17	58,487	0.06875	0.35	1.44413	1.39	0.15236	1.39	0.96	891	7	907	8	914	12	97
028-Z18	20,816	0.06950	0.90	1.46928	1.27	0.15335	1.27	0.95	914	18	918	8	920	11	99
029-Z19	178,299	0.06936	0.30	1.47021	1.33	0.15376	1.33	0.95	909	6	918	8	922	11	99
030-Z20	70,889	0.06946	0.43	1.44280	0.80	0.15067	0.80	0.89	912	9	907	5	905	7	101

Table 5
Summary of LA–ICP–MS data for Sample CHAP-DIOR.

Sample	Isotopic ratios								Ages						
	Pb^{206}/Pb^{204}	Pb^{207}/Pb^{206}	1σ (%)	Pb^{207}/U^{235}	1σ (%)	Pb^{206}/U^{238}	1σ (%)	Rho	Pb^{207}/Pb^{206}	1σ (Ma)	Pb^{207}/U^{235}	1σ (Ma)	Pb^{206}/U^{238}	1σ (Ma)	Conc (%)
003-Z01	29,480.5	0.061	1.048	0.853	1.447	0.102	0.998	0.671	622	23	626	7	627	6	101
004-Z02	32,584.3	0.061	1.066	0.852	1.563	0.101	1.142	0.718	638	23	626	7	622	7	97
005-Z03	52,629.2	0.061	0.774	0.856	1.118	0.102	0.807	0.693	642	17	628	5	624	5	97
006-Z04	22,973.4	0.062	2.636	0.849	3.022	0.100	1.479	0.724	663	56	624	14	613	9	93
012-Z06	13,441.8	0.061	0.723	0.803	1.031	0.095	0.735	0.677	647	16	598	5	585	4	90
013-Z07	19,858.1	0.061	0.732	0.813	1.062	0.096	0.769	0.692	654	16	604	5	591	4	90
014-Z08	23,488.7	0.062	2.009	0.830	2.270	0.098	1.057	0.679	663	43	614	10	600	6	91
017-Z09	34,239.3	0.062	0.804	0.829	1.167	0.098	0.846	0.699	663	17	613	5	600	5	91
018-Z10	13,307.6	0.062	1.148	0.805	1.747	0.095	1.317	0.745	660	25	600	8	584	7	88
019-Z11	37,486.9	0.061	0.747	0.816	1.048	0.097	0.735	0.665	644	16	606	5	596	4	93
020-Z12	17,680.7	0.064	3.087	0.893	3.287	0.101	1.128	0.563	740	65	648	16	622	7	84
023-Z13	63,459.6	0.061	0.942	0.839	1.568	0.099	1.253	0.790	656	20	619	7	609	7	93
024-Z14	108,724.8	0.061	0.554	0.828	0.826	0.098	0.613	0.690	645	12	612	4	604	4	94
025-Z15	94,884.4	0.061	0.683	0.813	1.062	0.096	0.814	0.740	652	15	604	5	592	5	91
026-Z16	24,568.2	0.070	3.138	0.985	3.641	0.103	1.847	0.747	914	65	696	18	631	11	69
029-Z17	29,975.0	0.060	0.885	0.854	1.228	0.103	0.852	0.667	598	19	627	6	635	5	106
030-Z18	294,933.5	0.061	0.596	0.918	1.289	0.110	1.143	0.879	626	13	661	6	672	7	107
031-Z19	40,911.2	0.061	0.796	0.884	1.229	0.104	0.936	0.743	657	17	643	6	639	6	97

Table 6
Sm–Nd isotopic data for representative rocks of the Chapada Cu–Au deposit.

Sample	Rock type	Sm (ppm)	Nd (ppm)	$^{147}Sm/^{144}Nd$	$^{143}Nd/^{144}Nd$	eNd (T)	TDM (Ga)
Chap-1	Equigranular metadiorite	3.69	17.45	0.128	0.512503	+4.94	0.96
Chap-179	Equigranular metadiorite	4.61	23.10	0.120	0.512484	+5.39	0.91
Chap-porf	Porphyritic metadiorite	2.65	12.96	0.124	0.512332	+2.29	1.20
Chap-2	Muscovite–biotite schist	4.39	19.05	0.139	0.512495	+3.52	1.12
Chap-10	Muscovite–biotite schist	3.88	17.03	0.138	0.512537	+4.51	1.01
Chap-1/6	Metabasalt	3.51	16.48	0.129	0.512530	+5.38	0.92
Cn-anf	Metabasalt	9.04	32.19	0.170	0.512779	+5.89	0.92
Chap-8	Metavolcaniclastic	1.86	9.84	0.115	0.512348	+3.38	1.06
Chap-12	Biotite–muscovite schist	1.73	8.07	0.129	0.512370	+2.17	1.21

metavolcanic/metasedimentary rocks, which exhibit a clear zonation with epidote-, amphibole-, biotite, and muscovite-rich rocks.

We suggest that these rocks were derived from the metamorphism superimposed on products generated during magmatic–hydrothermal alteration processes, similar to systems involved in the formation of porphyry Cu–Au deposits. The kyanite-rich rocks are associated with products of an advanced argillic hydrothermal alteration (argillic halo) rich in quartz and kaolinite (or pyrophyllite) (Fig. 3). Thus, growth of kyanite, as well as other aluminous minerals (staurolite, sillimanite, garnet), occurred during peak regional amphibolite facies metamorphism associated with D_n.

8.1.1. Hydrothermal alteration zoning

In surface mapping, the products associated with the advanced argillic alteration are more easily identified since they are represented by the association of kyanite- and muscovite-rich rocks that were resistant to the intense regional lateritic weathering. These rocks are widely distributed in the context of the Chapada Cu–Au deposit and, despite showing no direct association with copper mineralization, they may be indicative of its proximity (Fig. 3). The argillic alteration is commonly rich in pyrite and poor in chalcopyrite, and sporadically shows high concentrations of gold, which is therefore interpreted as an epithermal gold mineralization associated with advanced argillic lithocap.

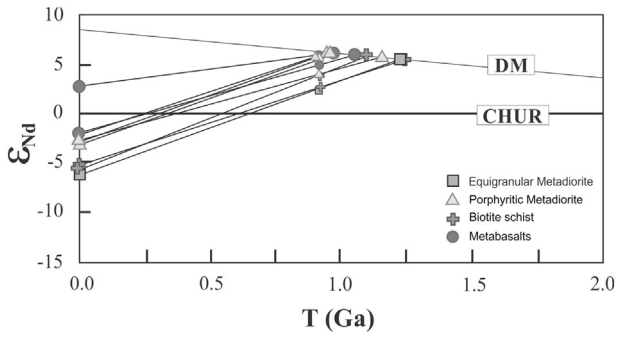

Fig. 11. Diagram εNd versus time showing Nd isotopic composition of the host rocks and wall rocks of the Chapada Deposit.

In contrast to the association of kyanite- and muscovite-rich rocks, the association of biotite-rich rocks, which are diagnostic of potassic hydrothermal alteration, is only identified in drill cores and in deeper levels of the open pit mine. Biotite is the dominant alteration mineral in schists (biotite-schist, amphibole–biotite schist, biotite–muscovite schist) whereas K-feldspar (microcline) increases in abundance in feldspathic biotite schists and biotite gneisses. Chalcopyrite and pyrite occur commonly associated with magnetite and the highest gold concentrations (Fig. 3).

Between the extremes of argillic and potassic alterations is the association of muscovite- and quartz-rich schists, with minor biotite, kyanite and epidote, which are interpreted as diagnostic of sericitic or phyllic alteration (Fig. 3). This association is rich in pyrite and, to a lesser extent, chalcopyrite.

The context surrounding the Chapada deposit contains association of amphibole- and epidote-rich rocks, ranging from epidosites to epidote amphibolites, which have been interpreted as representing the product of propylitic hydrothermal alteration. This association does not represent an important host rock of the Chapada Cu–Au deposit.

8.1.2. Ore mineral zoning

The Cu–Au ore consists of an association of disseminated sulfides (mainly chalcopyrite and pyrite) and oxides (magnetite, hematite, ilmenite, rutile), where chalcopyrite appears as the only important ore mineral.

The ore is represented predominantly by sulfide disseminations along foliation plans (or axial surfaces of folds) and to a lesser extent, in small massive concentrations in hinges of folds or EW and NW–SE oriented faults and fractures. In general, the ore is formed predominantly by chalcopyrite, pyrite and magnetite, where chalcopyrite–magnetite (magnetite-rich ore) and chalcopyrite–pyrite (pyrite-rich ore) are the prevailing associations, in which pyrite is the most abundant mineral, magnetite (including hematite, ilmenite and rutile) is subordinate, and galena, bornite, sphalerite and molybdenite are rarely reported. The two mineral associations are seen on detailed mapping of the open pit mine, where a core rich in magnetite (magnetite-rich ore) and an outer envelope where pyrite is predominant (pyrite-rich ore). The magnetite-rich core is predominantly hosted by biotite gneisses and biotite schists, described mainly in the NE portion of the pit mine, while the pyrite-rich ore is mainly associated with kyanite- and muscovite-rich schists exposed in the eastern and southwestern region of the open pit mine. The magnetite-rich ore contains more gold than the pyrite-rich ore.

8.1.3. Other typical porphyry-type features

In addition to the distinct hydrothermal alteration–mineralization zoning, the Chapada deposit shows other features that are usually identified in porphyry copper deposits. Among these features highlight deformed magnetite- and chalcopyrite-rich A-type quartz veins/veinlets associated with biotite-rich rocks (potassic hydrothermal alteration), A-type quartz vein with central suture of magnetite–chalcopyrite (Fig. 12a, b), as well as folded monomineralic lavender anhydrite veinlets/veins partially hydrated to gypsum which was subsequently dissolved and replaced by empty cavities (Fig. 12c,d).

In general, the Chapada Cu–Au deposit lacks typical porphyry-type structures and textures, such as breccias and crosscutting porphyry stocks and dykes, while veins and veinlets are abundant.

8.2. Shear zone-hosted Cu–Au mineralization

As discussed in the previous section, the Chapada Cu–Au deposit has features that largely resemble porphyry Cu–Au deposit deformed during D_n. However, in the northwestern sector of the deposit (Capacete sector), along to Chapada fault, the Cu–Au mineralization hosted in biotite–muscovite schist and magnetite–biotite gneiss and generated by epigenetic processes active during D_{n+1} has similarity to shear zone-hosted gold deposits (Fig. 3). These processes were responsible for retrograde metamorphism and metasomatic (?) reactions (biotitization, muscovitization, chloritization, carbonatization and sulfidation) related to the alteration of magnetite–biotite gneisses (equigranular metadiorite) into chalcopyrite- and pyrite-rich muscovite–biotite schists. The ore formed in this context is represented in different scales by neoformed biotite–muscovite domains, which envelops large volumes of preserved magnetite–biotite gneiss domains (Fig. 8b,c), ranging from few centimeters to tens of meters size (Fig. 13a,b). The sulfides (chalcopyrite, pyrite) display syn-kinematic planar dissemination, concordant with the low-angle mylonitic foliation (Fig. 13c,d), and occur interlayered with neoformed biotite and muscovite lamellar aggregates (Fig. 13e–g).

8.2.1. Mineralogical and geochemical modifications associated with shear zone-hosted mineralization

The mineralogical modifications that accompany the transformation of magnetite–biotite gneiss into muscovite–biotite schist during D_{n+1} are mainly evidenced by cryptic compositional variations of biotite, muscovite and plagioclase. In the preserved gneissic cores, biotite and muscovite are subordinate and occur most commonly as small lamellae dispersed in the granoblastic quartz–feldspathic domains. On the other hand, biotite and muscovite from newly formed schist occur as large lamellae with diablastic microstructure and, more commonly, concentrated in sulfide-rich micaceous domains that define the schistosity.

Neoformed biotite is slightly poorer in Ti, Mg and Al and more Fe-rich while neoformed muscovite is poorer in Ti and Al and richer in Mg and Fe (Table 7). Neoformed plagioclase is substantially poorer in the anorthite molecule and devoid of twinning, changing from oligoclase–andesine (An_{30}) to albite (An_5).

The geochemical changes are marked by variations in the content of several elements, among which copper, gold and sulfur stand out. The chemical analyses clearly show that while the preserved gneiss have very low concentration of these elements, the neoformed schist exhibits these elements at levels reaching up to about 0.37% Cu, 0.27 ppm Au and 3.33% S (Table 1, sample chap-10, Fig. 13a,b).

In the comparative situation illustrated in Fig. 13b, it is evident that the mineralogical and geochemical transformations that accompanied the deformation during D_{n+1} are the results of an important mineralization event. The very low concentrations of copper, gold and sulfur in the preserved gneiss suggests that these elements were most likely derived from an external source rather than by remobilization of juxtaposed magnetite–biotite gneiss.

9. Sulfur isotopic systematics

The first sulfur isotopic analyses of sulfides from the Chapada Cu–Au deposit were reported by Richardson et al. (1986). He reported a

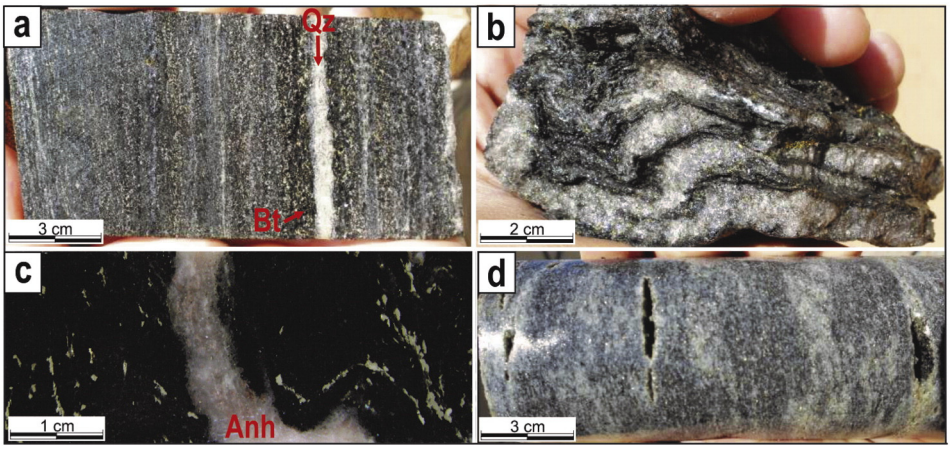

Fig. 12. (a) A-type quartz–chalcopyrite vein enveloped by hydrothermal biotite (potassic alteration). (b) Folded A-type quartz–chalcopyrite veins in equigranular metadiorite (biotite gneiss). (c) Folded lavender-colored anhydrite vein in pyrite-bearing muscovite–biotite schist. (d) Biotite gneiss-hosted former anhydrite vugs within A-type quartz veins/veinlets.

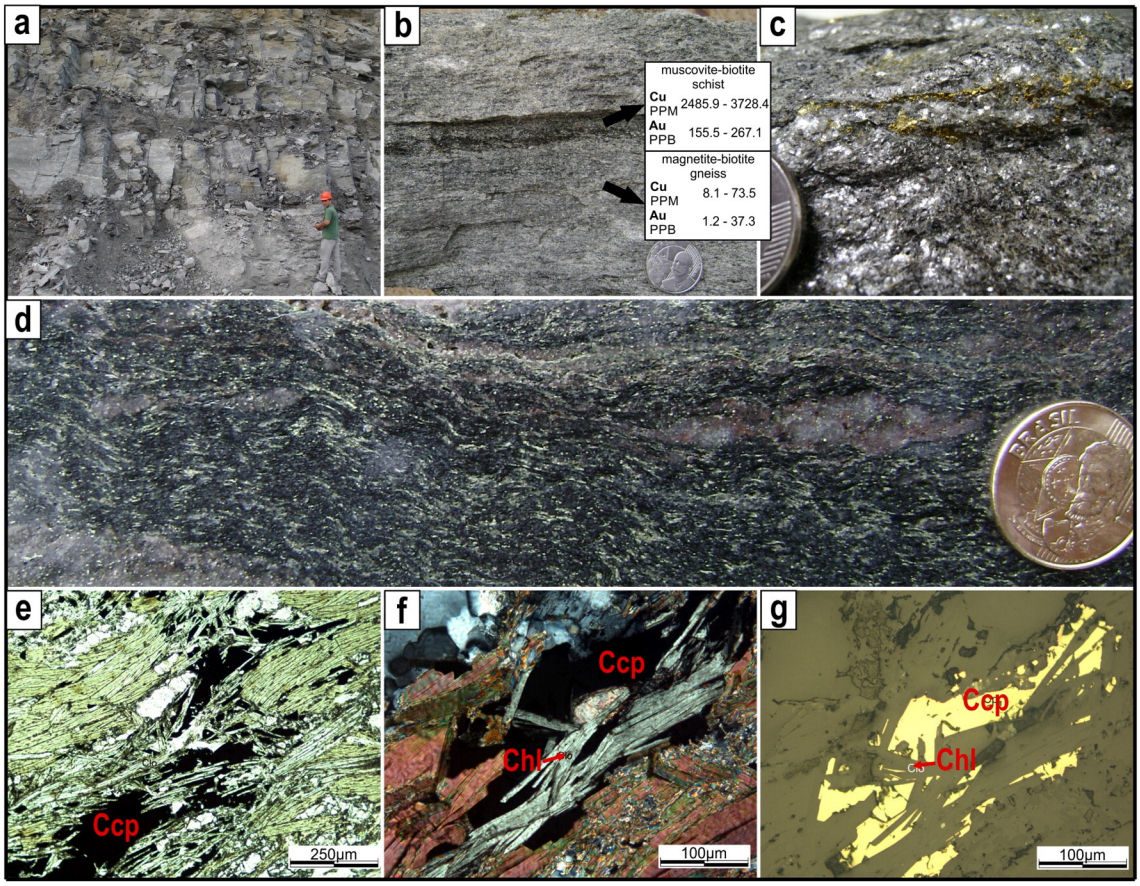

Fig. 13. Epigenetic mineralization associated with the deformational phase D_{n+1}. (a) Open pit exposure showing the relationship between magnetite–biotite gneiss (light gray) and muscovite–biotite schist (dark gray). (b) Detail of previous figure highlighting unmineralized magnetite–biotite gneiss interlayered with centimetric band of sulfide-rich muscovite–biotite schist. (c) Chalcopyrite and pyrite remobilized into hinge zone of folded muscovite–biotite schist. (d) Detail of the biotite schist showing concordant quartz segregation in a matrix composed also by biotite, quartz, plagioclase, epidote, chlorite and disseminations of chalcopyrite and pyrite. (e,f,g) Thin section photomicrograph (e: TL, N//; f: TL, NX; g: RL, N//) of the detail of pyrite and chalcopyrite interlayered with aggregates of neoformed biotite, muscovite and chlorite. Abbreviations are: TL — transmitted light; RL — reflected light; NX — crossed nicols; and N// — parallel nicols.

relatively narrow range of $\delta^{34}S$ values close to 0‰. In the present study, the average of $\delta^{34}S$ values in the Chapada sulfides (pyrite and chalcopyrite) are close to −1.0‰ (Table 8, Fig. 14). This strongly suggests that the sulfides were formed by fluids whose sulfur was derived from magmatic sources (Allègre, 2008; Ohmoto and Goldhaber, 1997). The ranges of $\delta^{34}S$ values of the Chapada sulfides (−2.90 to +0.76‰) are compatible with those of the majority of porphyry copper deposits (PCDs) whose $\delta^{34}S$ values of sulfides range from −3.0 to +1.0‰ (Ohmoto and Goldhaber, 1997). This isotopic homogeneity is consistent with a single reservoir or common source for the main stage hydrothermal fluids.

Table 7
Representative microprobe analysis of biotite from magnetite–biotite gneiss and muscovite–biotite schist of the Chapada Cu–Au deposit.

Rock	Magnetite–biotite gneiss			Sulfide-bearing muscovite–biotite schist		
Sample	Chap-1-1	Chap-1-3	Chap-1-5	Chap-4B-1	Chap-4B-2	Chap-4B-3
SiO_2	36.363	37.214	36.684	37.242	37.446	37.356
Al_2O_3	17.684	17.674	17.724	15.989	16.421	16.257
TiO_2	1.505	1.556	1.543	1.352	1.323	1.505
FeO	13.81	14.135	14.113	17.92	16.935	16.979
MnO	0.163	0.155	0.106	0.158	0.160	0.199
MgO	13.710	13.561	13.627	11.842	12.092	11.816
CaO	0.000	0.038	0.003	0.000	0.022	0.000
Na_2O	0.425	0.000	0.569	0.000	0.133	0.000
K_2O	9.712	9.927	9.790	9.759	9.983	9.980
BaO	0.189	0.068	0.153	0.000	0.000	0.000
Cl	0.151	0.031	0.039	0.240	0.150	0.105
H2O	3.912	3.987	3.971	3.852	3.904	3.898
Si	5.520	5.587	5.526	5.707	5.696	5.708
Ti	0.172	0.176	0.175	0.156	0.151	0.173
Al	3.164	3.127	3.147	2.888	2.944	2.928
Fe	1.753	1.775	1.778	2.296	2.154	2.170
Mn	0.021	0.020	0.014	0.020	0.021	0.026
Mg	3.102	3.034	3.060	2.705	2.742	2.691
Na	0.125	0.000	0.166	0.000	0.039	0.000
K	1.881	1.901	1.881	1.908	1.937	1.945
Ba	0.011	0.004	0.009	0.000	0.000	0.000

The range of $\delta^{34}S$ values of sulfides (pyrite and chalcopyrite) from Chapada is in conformity with the ranges of $\delta^{34}S$ values for sulfides from individual hydrothermal alteration haloes of the porphyritic mineralization event, which are relatively similar to each other (propylitic alteration: −2.90 to +0.75‰, potassic alteration: −2.32 to +0.07‰, phyllic alteration: −2.28 to 0.07‰, argillic alteration: −2.90 to 0.76‰) (Fig. 14). The epigenetic mineralization event, represented by the biotitic hydrothermal alteration (or biotitization), also shows sulfur isotopic composition of sulfides in this narrow interval (−1.79 to +0.74‰) (Fig. 14). Thus, one can accept that both the porphyry mineralization and the epigenetic mineralization were generated by sulfur of magmatic origin (Fig. 14).

10. Discussion and conclusion

10.1. Tectonic setting of the Chapada Cu–Au deposit

The Goiás Magmatic Arc may be identified as part of an accretionary orogen with tectonic evolution between 900 and 600 Ma during the Brasiliano Orogeny. According to Hronsky et al. (2012), such

Table 8
Sulfur isotope results obtained in sulfides from the hydrothermal alteration haloes of the Chapada Cu–Au deposit.

Sample	Hydrothermal alteration	Mineral	$\delta^{34/32}S$(‰) VCDT
Chap-12	Propylitic	Chalcopyrite	−2.90
Chap-14	Propylitic	Pyrite	−1.30
Chap-13	Propylitic	Pyrite	−1.26
Chap-07	Propylitic	Pyrite	−0.88
Chap-22	Propylitic	Pyrite	−0.15
Chap-19	Propylitic	Pyrite	−0.11
Chap-5	Propylitic	Pyrite	+0.75
Chap-15	Phillic	Chalcopyrite	−2.28
Chap-08	Phillic	Chalcopyrite	−1.20
Chap-24	Phillic	Chalcopyrite	−0.50
Chap-17	Phillic	Pyrite	+0.07
Chap-11	Argillic	Chalcopyrite	−2.90
Chap-10	Argillic	Pyrite	−1.86
Chap-21	Argillic	Pyrite	−0.53
Chap-06	Argillic	Pyrite	+0.76
Chap-16	Potassic	Chalcopyrite	−2.32
Chap-09	Potassic	Pyrite	−1.82
Chap-23	Potassic	Chalcopyrite	−1.14
Chap-20	Potassic	Pyrite	−0.30
Chap-18	Potassic	Pyrite	+0.07
Chap-30	Biotitization	Chalcopyrite	−1.77
Chap-32	Biotitization	Chalcopyrite	−1.63
Chap-31	Biotitization	Chalcopyrite	−1.48
Chap-29	Biotitization	Chalcopyrite	−1.28
Chap-38	Biotitization	Chalcopyrite	−1.02
Chap-34	Biotitization	Chalcopyrite	−0.95
Chap-36	Biotitization	Chalcopyrite	−0.86
Chap-33	Biotitization	Chalcopyrite	−0.85
Chap-26	Biotitization	Chalcopyrite	−0.83
Chap-35	Biotitization	Chalcopyrite	−0.70
Chap-27	Biotitization	Chalcopyrite	−0.68
Chap-28	Biotitization	Chalcopyrite	−0.66
Chap-37	Biotitization	Chalcopyrite	−0.49
Chap-25	Biotitization	Chalcopyrite	−0.46
Chap-47	Biotitization	Chalcopyrite	−0.35
Chap-48	Biotitization	Chalcopyrite	−0.28
Chap-50	Biotitization	Chalcopyrite	−0.23
Chap-54	Biotitization	Chalcopyrite	−0.23
Chap-49	Biotitization	Chalcopyrite	−0.22
Chap-39	Biotitization	Chalcopyrite	−0.18
Chap-40	Biotitization	Chalcopyrite	−0.11
Chap-52	Biotitization	Chalcopyrite	−0.09
Chap-44	Biotitization	Chalcopyrite	−0.06
Chap-42	Biotitization	Chalcopyrite	−0.03
Chap-43	Biotitization	Chalcopyrite	−0.03
Chap-53	Biotitization	Chalcopyrite	−0.02
Chap-51	Biotitization	Chalcopyrite	+0.02
Chap-41	Biotitization	Chalcopyrite	+0.17
Chap-45	Biotitization	Chalcopyrite	+0.62
Chap-46	Biotitization	Chalcopyrite	+0.74

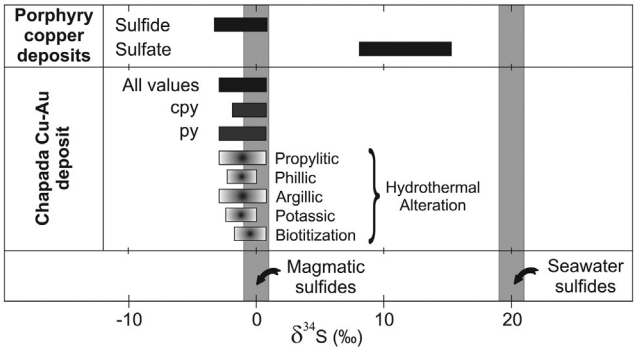

Fig. 14. Sulfur isotopic composition of sulfides from hydrothermal alteration haloes of the Chapada Cu–Au deposit compared with some important sulfur reservoirs (modified from Allègre (2008)).

accretionary orogens are characterized by broad zones of complex geology, incorporating many distinctive geological domains, including accretionary wedges, island arcs, continental fragments, clastic sedimentary basins and overprinting magmatic belts. Mineral deposits in accretionary orogens can be subdivided, on the basis of their spatial and temporal distributions within an evolving convergent plate margin scenario, into: a) those that are related to the continental (or intra-oceanic) magmatic arcs themselves or constructional stage; b) those that develop in arc-flanking environments such as in the evolving fore-arc, back-arc or far back-arc portions of accretionary systems during deformation, burial and exhumation of the continental margin or orogenic stage; and c) those that form in more distal foreland basin settings or late orogenic to post-orogenic stage (Bierlein et al., 2009; Groves and Bierlein, 2007; Kesler, 1997; Richards, 2011).

At the district scale (ca. 120 km long), the Chapada Cu–Au deposit, as well as other minor porphyry Cu–Au deposits that compose of Chapada-Mara Rosa Cu–Au district, occur as linear alignments oriented parallel to the Mara Rosa magmatic arc trend, which are marked by narrow and linear ridges in which kyanite-rich rocks outcrop (Fig. 15). As discussed before, these rocks probably represent former advanced hydrothermal alteration product (advanced argilic halo) overprinted by greenschist to amphibolite facies metamorphism conditions. According to various authors (e.g. Sillitoe, 2010), arc-parallel alignments may occur along intra-arc fault zones (or intra-arc fault system), active before as well as during magmatism and porphyry Cu generation, are invariably involved, to greater or lesser degrees, in determining the formational sites and geometries of porphyry Cu systems and their constituent parts, including sub-epithermalZn–Cu–Pb–Ag ± Au veins, high-sulfidation epithermal Cu–Au ± Ag deposits, proximal Cu–Au skarns, distal Au–Zn–Pb skarns, intermediate sulfidation epithermal disseminated Au ± Ag ± Cu deposits and distal sediment-hosted disseminated Au–As ± Sb ± Hg deposits.

The NNEarc-parallel alignments and their coincident porphyry Cu–Au deposits and occurrences are disrupted by dextral EW-transverse lineaments that may represent former reactivated cross-arc faults (Fig. 15). Although these faults are not directly associated with Cu–Au mineralization, some authors emphasize the importance of intersections between continent-scale transverse fault zones or lineaments and arc-parallel structures for porphyry Cu formation (e.g. Tosdal and Richards, 2001; Sillitoe, 2010).

The Chapada deposit, as well as most of the Cu–Au deposits and occurrences in the region, show close spatial, temporal, and genetic relationships with the interface between cupolas of equigranular and porphyriticmedium- to high-Kcalc-alkaline metadiorites, with ages from 884 ± 15 to 867 ± Ma, and basic to intermediate metavolcanic/metapyroclastic and metavolcanoclastic rocks, with ages from 930 to 890 Ma, probably generated in active subduction-related arc magmatism (including backarc). In general, the geological context of the deposit lacks preserved porphyry intrusions, stocks and dykes. At the same time, the elongated geometry of the kyanite-rich rocks suggests that these rocks are associated with the formation of former advanced argillic lithocaps over porphyry dyke-like bodies (Fig. 15), whose were overprinted by greenschist to amphibolite facies metamorphic conditions.

10.2. Significance of the kyanite-rich rocks

Recently, some authors (e.g. Müller et al., 2007; Owens and Pasek, 2007) have reviewed the genetic significance of kyanite-rich rocks generated in geological context similar to that described in the Mara Rosa magmatic arc. The conclusions presented by these authors are in accordance with the results obtained in the present study. Müller et al. (2007) suggest that the protoliths of the kyanite quartzites from Norway are the products of metamorphosed advanced argillic alteration zones in felsic and intermediate volcanic and subvolcanic rocks of island arc settings, while Owens and Pasek (2007) report evidence that the

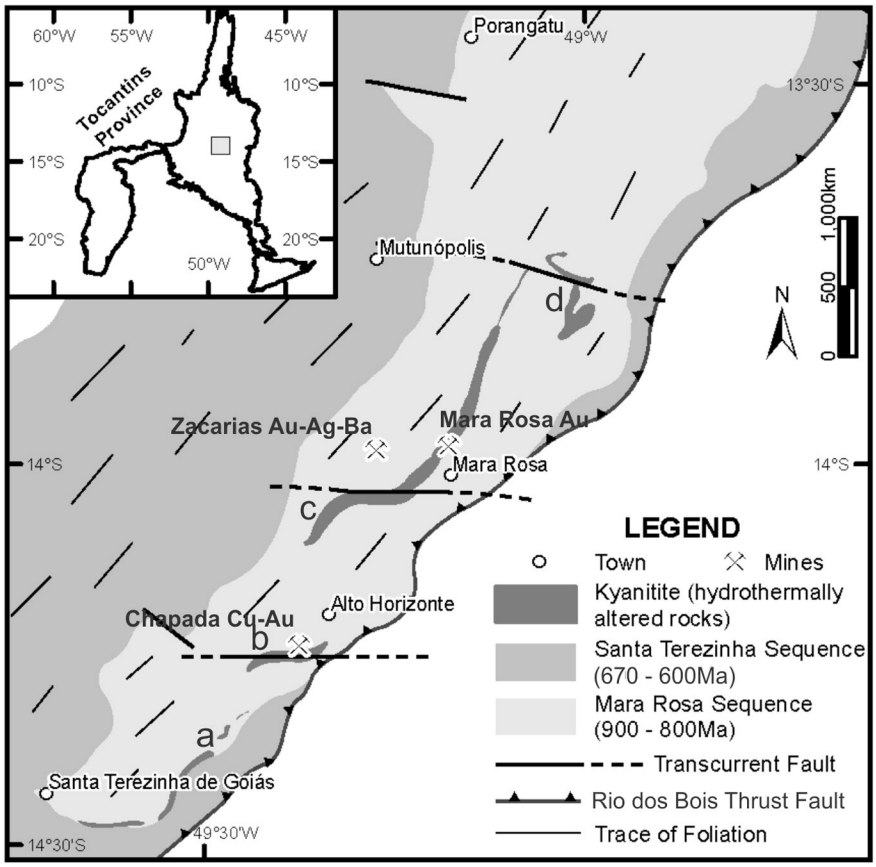

Fig. 15. Simplified geological map of the Mara Rosa magmatic arc showing kyanite-rich rock clusters and alignments of various sizes and morphologies. There is a spatial coincidence between the copper and/or gold occurrences and deposits, including Chapada Cu–Au deposit, and the former advanced hydrothermal alteration zones identified by kyanite-rich rocks, which can also coincide with an intra-arc fault zone. Kyanite-rich ridges: a. Serra das Araras; b. Morro do Urubu; c. Serra de Bom Jesus; and d. Serra do Caranã.

protoliths of the kyanite quartzites from Piedmont Province in Central Virginia (USA), where the world's largest kyanite mines are located, originated by severe leaching (advanced argillic alteration) in a high-sulfidation epithermal gold system. Similarly to the Chapada deposit, these kyanite quartzites also contain accessory rutile, muscovite and locally abundant pyrite (±gold). Corundum, lazulite, roscoelite and other rare minerals occur in some samples (Müller et al., 2007; Owens and Pasek, 2007).

10.3. Potassic hydrothermal alteration versus biotitic alteration

In spite of intense deformation and metamorphism, the Chapada deposit displays a consistent, broad-scale alteration zoning pattern, mainly observed in the Corpo Sul orebody, that comprises, centrally from the bottom upward, potassic, sericitic and argillic zones, analogous to those associated with preserved porphyry-type Cu–Au deposits.

While the argillic hydrothermal alteration may be inferred directly from the kyanite-rich metamorphic assemblages, as discussed above, the biotite-rich metamorphic assemblage does not always represent metamorphosed product formed of potassic hydrothermal alteration analogous to that associated with porphyry-type Cu–Au deposits. Biotite-rich rocks were also generated during D_{n+1}, which involved the transformation of magnetite–biotite gneiss (or equigranular metadiorite) to muscovite–biotite schist, a process here called biotitization (biotitic alteration).

In the Chapada deposit, spatial distribution, assemblages and textures of metamorphosed potassic alteration are quite distinct from those of the biotitic alteration since in potassic alteration zones, igneous biotite is itself altered to more Mg-rich and Ti-poor compositions. Fe released during biotite alteration is generally fixed by hydrothermal sulfur, resulting in the development of intergrown clusters of hydrothermal Mg–biotite, titanite, and pyrite. In biotitic alteration (or biotitization), metamorphic biotite from the magnetite–biotite gneiss (or equigranular metadiorite) is itself altered to more Fe-rich and Ti-poor compositions. Fe released during magnetite alteration is fixed by both sulfur and newly formed hydrothermal biotite, resulting in the development of lamellar intergrowth of hydrothermal Fe–biotite, chalcopyrite and pyrite.

10.4. Porphyry-type and shear zone-hosted Cu–Au mineralizations

Several genetic models have been suggested for Chapada, including (i) a deformed and metamorphosed porphyry-type Cu–Au deposit (Richardson et al., 1986), (ii) a deformed and metamorphosed volcanogenic disseminated sulfide deposit (Silva and Sá, 1986; Kuyumjian, 1989), and (iii) epithermal Cu–Au deposit overprinted by metamorphic remobilization (Kuyumjian, 2000). In this work, we proposed a two-stage model that includes an early porphyry-typeCu–Au mineralization overprinted by a syn-deformational Cu–Au mineralization (shear zone-hosted mineralization), which may represent an orogenic Cu–Au mineralization or an intrusion-related Cu–Au mineralization (Fig. 16a–c).

The early mineralization event, which pre-date the peak regional amphibolite-facies metamorphism of D_n(650 °C and 9 kbar), is associated with deformed and metamorphosed Neoproterozoic porphyry-type deposit (884 to 867 Ma). Several features are consistent with a magmatic–hydrothermal model, including: contemporaneous emplacement of intrusive suites (equigranular and porphyritic diorites) and formation of Cu–Au mineralization; a preserved hydrothermal alteration zoning

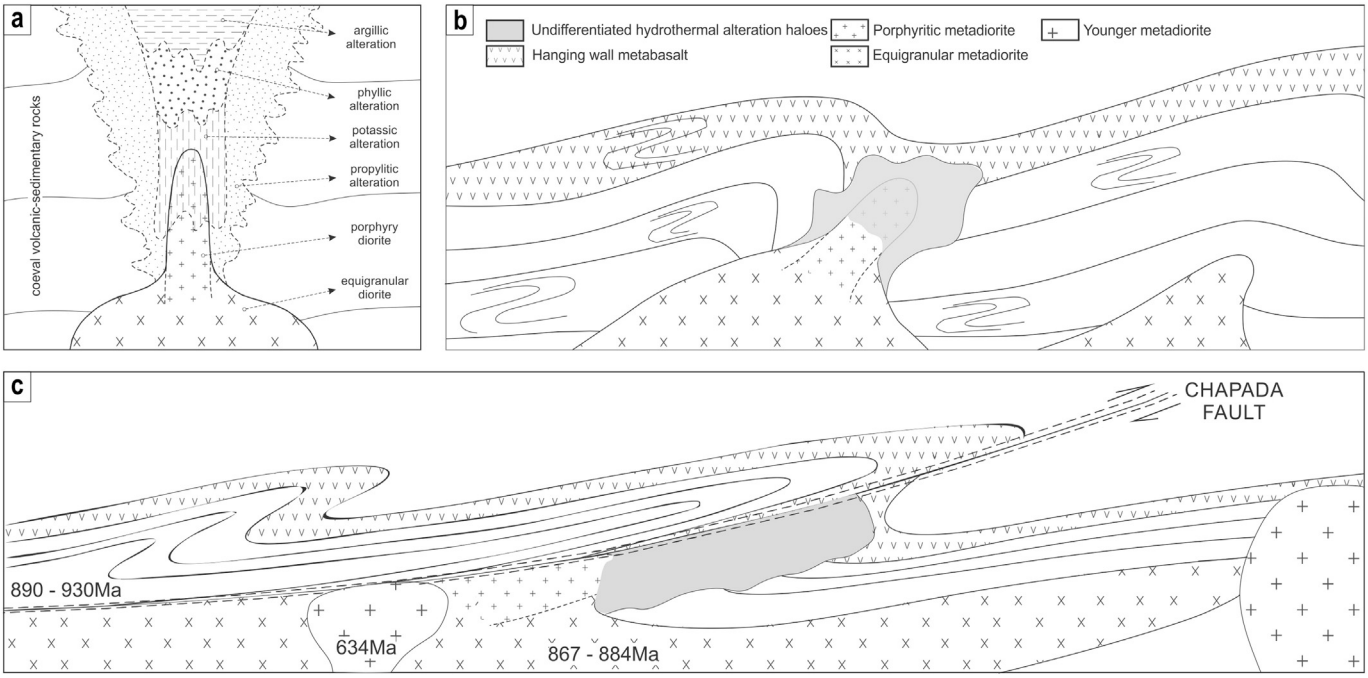

Fig. 16. Not-to-scale sections illustrating the relationship between intrusions, hydrothermal alteration, Cu–Au mineralization and structural evolution of the Chapada Cu–Au deposit: (a) Schematic and hypothetical distribution of magmatic–hydrothermal alteration assemblages developed during porphyry mineralization stage. (b) Schematic section highlighting the relationship between the wall rocks, intrusions and porphyry Cu–Au mineralization deformed by crustal shortening during early D_n. (c) Schematic section of the syn-epigenetic mineralization stage during D_{n+1} illustrating tightening of folds, development of thrust faults and pluton intrusion.

which highlights the potassic and argillic alterations diagnosed by metamorphic assemblages rich in biotite and kyanite, respectively; a systematic oxide/sulfide zonation around the deposit, including the peripheral pyritic shell and the central magnetite-rich zone. The highest concentrations of copper and gold are associated with domains rich in magnetite. Chalcopyrite is the main ore mineral and shows evidences of intense deformation/recrystallization.

The later mineralization event is associated with a shear zone-hosted Cu–Au deposit coeval with the development of the Rio dos Bois thrust to reverse fault during D_{n+1}. This event would have occurred between 630 and 580 Ma during the late orogenic to post-orogenic stage of the Mara Rosa magmatic arc.This context was marked by hydrothermal alteration or local retrogression to greenschist-facies metamorphism (460 °C and 5 kbar) which is mainly evidenced by the transformation of magnetite–biotite gneisses into muscovite–biotite schists and amphibolite into amphibole–chlorite–epidote schist. Several features are consistent with a metamorphic-hydrothermal model, including: the Cu–Au mineralization is coeval with retrograde metamorphic assemblages (biotite–muscovite–epidote–albite) of greenschist facies generated during D_{n+1}; mineralized ore zone shows subhorizontal to low angle tabular geometry in concordance with the thrust fault plane or milonitic foliation; sulfides (chalcopyrite, pyrite) and newly formed biotite/muscovite occur in interlayered arrangements (lamellar intergrowth) and show no evidence of overprinted deformation and/or recrystallization. The features are in part compatible with either orogenic gold systems or intrusion-related systems (Groves et al., 1998; Bierlein et al., 2009; Hart, 2007). Both systems display a wide variety of mineralization styles that depend on the (i) depth of intrusion, emplacement and gold (metals) deposition, (ii) distance from the parent intrusion, and (iii) structural controls (Thompson and Newberry, 2000). On the one hand most of the features presented are compatible with orogenic gold systems, however there are no reports in the literature linking elevated copper concentrations in these systems. Thus, this fact leads us to suggest a mineralization model with characteristics intermediate between the two systems, compatible with a distal intrusion-related system (Fig. 16). In this case, the younger metadiorites, dated to 634.8 ± 6.8 Ma, could have played an important role in the Chapada Cu–Au mineralization.

Acknowledgments

The University of Brasília is gratefully acknowledged for fieldwork support and access to laboratory facilities. We thank the Yamana Gold Inc. and the Brazilian Council for Research and Technological Development (CNPQ)for providing, respectively, logistical and financial support for this study. The authors also thank the geologists Carlos Eduardo Paraízo Borges, Emerson Oliveira Ramos, Leandro Duarte Campos and Patricia Tatiane Lopes, for their fieldwork and mine assistance. Finally, we are indebted to anonymous reviewers for their helpful review of the original manuscript.

References

Albarède, F., Telouk, P., Blichert-Toft, J., Boyet, M., Agranier, A., Nelson, B., 2004. Precise and accurate isotopic measurements using multiple collector ICPMS. Geochim. Cosmochim. Acta 68, 2725–2744.
Allègre, C.J., 2008. Isotope Geology. Cambridge University Press (512 pp.).
Allibone, A.H., Windh, J., Etheridge, M.A., Burton, D., Anderson, G., Edwards, P.W., Miller, A., Graves, C., Fanning, C.M., Wysoczanski, 1998. Timing relationships and structural controls on the location of Au–Cu mineralization at the Boddington gold mine, Western Australia. Econ. Geol. 93, 245–270.
Arantes, D., Buck, P.S., Osbourne, G.A., Porto, C.G., 1991. A Sequência vulcano-sedimentar de Mara Rosa e mineralizações auríferas associadas. Boletim Informativo da SBG, Núcleo Centro-Oeste, pp. 27–40 (in Portuguese).
Araújo Filho, J.O., 2000. The Pirineus syntaxis: an example of intersection of two Brasiliano fold thrust belts in Central Brazil, and its implications for the tectonic evolution of Western Gondwana. Rev. Bras. Geosci. 30, 144–148.
Ayres, L.D., Averill, S.A., Wolfe, W.J., 1982. An Archean molybdenite occurrence of possible porphyry type at Setting Net Lake, Northwestern Ontario, Canada. Econ. Geol. 77, 1105–1119.
Bendall, C., Lahaye, Y., Fiebig, J., Weyer, S., Brey, G.P., 2006. In situ sulfur isotope analysis by laser ablation MC–ICPMS. Appl. Geochem. 21, 782–787.
Bierlein, F.P., Groves, D.I., Cawood, P.A., 2009. Metallogeny of accretionary orogens — the connection between lithospheric processes and metal endowment. Ore Geol. Rev. 36, 282–292.
Boynton, W.V., 1984. Cosmochemistry of the rare-earth elements: meteorite studies. In: Henderson, P. (Ed.), Rare-Earth Elements Geochemistry. Elsevier, Amsterdam, pp. 63–114.

Buhn, B., Pimentel, M.M., Matteini, M., Dantas, E.L., 2009. High spatial resolution analysis of Pb and U isotopes for geochronology by laser ablation multi-collector inductively coupled plasma mass spectrometry (LA–MC–ICP–MS). An. Acad. Bras. Cienc. 81, 99–114.
Cooke, D.R., Hollings, P., 2005. Giant porphyry deposits: characteristics, distribution, and tectonic controls. Econ. Geol. 100, 801–818.
Defant, M.J., Drummond, M.S., 1993. Mount St. Helens: potential example of the partial melting of the subducted lithosphere in a volcanic arc. Geology 21, 547–550.
DePaolo, D.J., 1981. A neodymium and strontium isotopic study of the Mesozoic calc-alkaline granitic batholiths of the Sierra Nevada and Peninsular Ranges. Calif. J. Geophys. Res. 86, 10470–10488.
Ding, T., Valkiers, S., Kipphardt, H., De Bièvre, P., Taylor, P.D.P., Gonfiantini, R., Krouse, R., 2001. Calibrated sulfur isotope abundance ratios of three IAEA sulfur isotope reference materials and V-CDT with a reassessment of the atomic weight of sulfur. Geochim. Cosmochim. Acta 65, 2433–2437.
Duuring, P., Kassidy, K.F., Hagemann, S.G., 2007. Granitoid-associated orogenic, intrusion-related and porphyry style metal deposits in the Archean Yilgarn Craton, Western Australia. Ore Geol. Rev. 32, 157–186.
Fraser, R.J., 1993. The Lac Troilus gold–copper deposit, northwestern Quebec: a possible Archean porphyry system. Econ. Geol. 88, 1685–1699.
Frost, B.R., Barnes, C.G., Collins, W.J., Arculus, R.J., Ellis, D.J., Frost, C.D., 2001. A geochemical classification for granitic rocks. J. Petrol. 42, 2033–2048.
Fuck, R.A., Pimentel, M.M., D'el Rey Silva, L.J.H., 1994. Compartimentação tectônica da porção oriental da Província Tocantins. Anais, 38o. Congresso Brasileiro de Geologia, Balneário Camburiú-SC, pp. 215–216 (in Portuguese).
Gaal, G., Isohanni, 1979. Characteristics of igneous intrusions and various wall rocks in some Precambrian porphyry copper–molybdenum deposits in Pohjanmaaa, Finland. Econ. Geol. 74, 1198–1210.
Gioia, S.M.C.L., Pimentel, M.M., 2000. The Sm–Nd isotopic method in the geochronology laboratory of the University of Brasília. An. Acad. Bras. Cienc. 72 (2), 219–245.
Giustina, M.E., Oliveira, C.G., Pimentel, M.M., Bernhard, B., 2009. Neoproterozoic magmatism and high-grade metamorphism in the Goiás Massif: new LA–MC–ICMPS U–Pb and Sm–Nd data and implications for collisional history of the Brasília Belt. Precambrian Res. 172, 67–79.
Groves, D.I., Bierlein, F.P., 2007. Geodynamic settings of mineral deposit systems. J. Geol. Soc. Lond. 164, 19–30.
Groves, D.I., Goldfarb, R.J., Gebre-Mariam, M., Hagemann, S.G., Robert, F., 1998. Orogenic gold deposits: a proposed classification in the context of their crustal distribution and relationship to other gold deposit types. Ore Geol. Rev. 13, 7–27.
Gustafson, L.B., 1978. Some major factors of porphyry copper genesis. Econ. Geol. 73, 600–607.
Hart, C.J.R., 2007. Reduced intrusion-related gold systems. In: Goodfellow, W.D. (Ed.), Mineral deposits of Canada: A Synthesis of Major Deposit Types, District Metallogeny, the Evolution of Geological Provinces, and Exploration Methods: Geological Association of Canada, Mineral Deposits Division. Special Publication N 5, pp. 95–112.
Hou, Z., Zhang, H., Pan, X., Yang, Z., 2011. Porphyry Cu (–Mo–Au) deposits related to melting of thickened mafic lower crust: examples from the eastern Tethyan metallogenic domain. Ore Geol. Rev. 39, 21–45.
Hronsky, J.M.A., Groves, D.I., Loucks, R.R., 2012. A unified model for gold mineralisation in accretionary orogens and implications for regional scale exploration targeting methods. Mineral. Deposita 47, 339–358.
Irvine, T.N., Baragar, W.R., 1971. A guide to the chemical classification of the common volcanic rocks. Can. J. Earth Sci. 8, 523–548.
Jackson, S.E., Pearson, N.J., Griffin, W.L., Belousova, E.A., 2004. The application of laser ablation-inductively coupled plasma-mass spectrometry. Chem. Geol. 211, 47–69.
Junges, S.L., Pimentel, M.M., Moraes, R., 2002. Nd isotopic study of the Neoproterozoic Mara Rosa Arc, central Brazil: implications for the evolution of the Brasília Belt. Precambrian Res. 117 (1–2), 101–108.
Kesler, S.E., 1997. Metallogenic evolution of convergent margins: selected ore deposit models. Ore Geol. Rev. 12, 153–171.
Kesler, S.E., Wilkinson, B.H., 2006. The role of exhumation in the temporal distribution of ore deposits. Econ. Geol. 101, 919–922.
Kuyumjian, R.M., 1989. The geochemistry and tectonic significance of amphibolites from the Chapada sequence, central Brazil. Unpublished PhD thesis, University of London, 289 pp.
Kuyumjian, R.M., 1995. Diversity of fluids in the origin of the Chapada Cu–Au deposit, Goiás. Rev. Bras. Geosci. 25 (3), 203–205.
Kuyumjian, R.M., 2000. Magmatic arc and associated gold, copper, silver and barite deposits in the State of Goiás, Central Brasil: characteristics and speculations. Rev. Bras. Geosci. 30, 285–288.
Lang, J.R., Stanley, C.R., Thompson, J.F.H., Dunne, K.P.E., 1995. Na–K–Ca magmatic–hydrothermal alteration in alkalic porphyry Cu–Au deposits. British Columbia: Mineralogical Association of Canada Shortcourse 23, pp. 339–366.
Laux, J.H., Pimentel, M.M., Dantas, E.L., Armstrong, R., Junges, S.L., 2005. Two Neoproterozoic crustal accretion events in the Brasília Belt, central Brazil. J. S. Am. Earth Sci. 18, 183–198.
Le Bas, M.J., Le Maitre, R.W., Streckeisen, A., Zanettin, B., 1986. A chemical classification of volcanic rocks based on the total alkali-silica diagram. J. Petrol. 27, 745–750.
Ludwig, K.R., 2003. Isoplot 3.00: A Geochronological Toolkit for Microsoft Excel. Berkeley Geochronological Center, Special Publication 4 (70 pp.).
Mason, P.R.D., Košler, J., de Hoog, J.C.M., Sylvester, P.J., Meffan-Main, S., 2006. In situ determination of sulfur isotopes in sulfur-rich materials by laser ablation multiple collector inductively coupled plasma mass spectrometry (LA–MC–ICP–MS). J. Anal. At. Spectrom. 21, 177–186.
McCuaig, T.C., Behn, M., Stein, H.J., Hagemann, S.G., McNaughton, N.J., Cassidy, K.F., Champion, D., Wyborn, L., 2001. The Boddington gold mine: a new style of Archaean Au–Cu deposit. AGSO-GeoscienceAustralia. Record 2001/37, pp. 453–455.
Meyer, C., Hemley, J.J., 1967. Wall rock alteration. In: Barnes, H.L. (Ed.), Geochemistry of Hydrothermal Ore Deposits. Holt, Rinehart and Winston, New York, pp. 166–235.
Minnit, R.C.A., 1986. Porphyry Copper, Molybdenum Mineralization at Haib River, Southwest Africa/Namibia. Mineral Deposits of Southern Africa, Geologic Society of South Africa 2, pp. 1567–1585.
Mitchell, A.H., Garson, M.S., 1972. Relationship of porphyry copper and circum-Pacific tin deposits to palaeo-Benioff zones. Trans. Inst. Min. Metall. 81, B10–25.
Morrison, G.W., 1980. Characteristics and tectonic setting of the shoshonite rock association. Lithos 13, 97–108.
Müller, A., Ihlen, P.M., Wanvik, J.E., Flem, B., 2007. High-purity quartz mineralisation in kyanite quartzites, Norway. Mineral. Deposita 42, 523–535.
Ohmoto, H., Goldhaber, M.B., 1997. Sulfur and carbon isotopes. In: Barnes, H.L. (Ed.), Geochemistry of Hydrothermal Ore Deposits. J Wiley and Sons, pp. 517–611.
Oliveira, C.G., Queiroz, C.L., Pimentel, M.M., 2000. The Arenópolis-Mara Rosa gold–copper belt, Neoproterozoic Goiás Magmatic Arc. Rev. Bras. Geosci. 30, 219–221.
Oliveira, C.G., Pimentel, M.M., Melo, L.V., Fuck, R.A., 2004. The Cooper–gold and gold deposits of the Neoproterozoic Mara Rosa magmatic arc, central Brazil. Ore Geol. Rev. 25, 285–299.
Oliveira, C.G., Oliveira, F.B., Dantas, E.L., Fuck, R.A., Della Giustina, M.E.S., 2006. Programa Geologia do Brasil-Folha Campinorte. FUB/CPRM, Brasília (124 pp. (in Portuguese)).
Owens, B.E., Pasek, M.A., 2007. Kyanite quartzites in the Piedmont Province of Virginia: evidence for a possible high-sulphidation system. Econ. Geol. 102, 495–509.
Pearce, J.A., Harris, N.B.W., Tindle, A.G., 1984. Trace element discrimination diagrams for the tectonic interpretation of granitic rocks. J. Petrol. 25, 956–983.
Pimentel, M.M., Whitehouse, M.J., Viana, M.G., Fuck, R.A., Machado, N., 1997. The Mara Rosa Arc in the Tocantins Province: further evidence for Neoproterozoic crustal accretion in central Brazil. Precambrian Res. 81, 299–310.
Richards, J.P., 2003. Tectono-magmatic precursors for porphyry Cu–(Mo–Au) deposit formation. Econ. Geol. 98, 1515–1533.
Richards, J.P., 2005. Cumulative factors in the generation of giant calc-alkaline porphyry Cu deposits. In: Porter, T.M. (Ed.), Super porphyry Copper and Gold Deposits: A Global Perspective, v. 1. PGC Publishing, Adelaide, pp. 7–25.
Richards, J.P., 2011. Magmatic to hydrothermal metal fluxes in convergent and collided margins. Ore Geol. Rev. 40, 1–26.
Richards, J.P., Kerrich, R., 2007. Adakite-like rocks: their diverse origins and questionable role in metallogenesis. Econ. Geol. 102, 537–576.
Richardson, S.V., Kesler, S.E., Essene, E.J., 1986. Origin and geochemistry of the Chapada Cu–Au deposit, Goiás, Brazil: a metamorphosed wall-rock porphyry copper deposit. Econ. Geol. 81, 1884–1898.
Roth, E., Groves, D., Anderson, G., Daley, L., Staley, R., 1991. Primary mineralization at the Boddington Gold Mine, Western Australia: an Archean porphyry Cu–Au–Mo deposit. In: Ladeira, E.A. (Ed.), Symposium Brazil Gold'91, pp. 481–488.
Sarkar, S.C., Kabiraj, S., Bhattacharya, S., Pal, A.B., 1996. Nature, origin and evolution of the granitoid-hosted Early Proterozoic copper–molybdenum mineralization at Malanjkhand, Central India. Mineral. Deposita 31, 419–431.
Seedorff, E., Dilles, J.H., Proffett Jr., J.M., Einaudi, M.T., Zurcher, L., Stavast, W.J.A., Johnson, D.A., Barton, M.D., 2005. Porphyry deposits: characteristics and origin of hypogene features. Economic Geology 100th anniversary volume, pp. 251–298.
Seedorff, E., Barton, M.D., Stavast, W.J.A., Maher, D.J., 2008. Root zones of porphyry systems: extending the porphyry model to depth. Econ. Geol. 103, 939–956.
Sikka, D.B., Nehru, C.E., 2002. Malanjkhand copper deposit, India: is it not a porphyry type? J. Geol. Soc. India 59, 339–362.
Sillitoe, R.H., 1997. Characteristics and controls of the largest porphyry copper–gold and epithermal gold deposits in the circum-Pacific region. Aust. J. Earth Sci. 44, 373–388.
Sillitoe, R.H., 1998. Major Regional Factors Favoring Large Size, High Hypogene Grade, Elevated Gold Content and Supergene Oxidation and Enrichment of Porphyry Copper Deposits. In: Porter, T.M. (Ed.), Porphyry and Hydrothermal Copper and Gold Deposits: A Global Perspective, Perth, 1998. Conference Proceedings: Glenside, South Australia, Australian Mineral Foundation, pp. 21–34.
Sillitoe, R.H., 2000. Gold-rich porphyry deposits: descriptive and genetic models and their role in exploration and discovery. Rev. Econ. Geol. 13, 315–345.
Sillitoe, R.H., 2008. Major gold deposits and belts of the North and South American Cordillera: distribution, tectonomagmatic settings, and metallogenic considerations. Econ. Geol. 103, 663–687.
Sillitoe, R.H., 2010. Porphyry copper systems. Econ. Geol. 105, 3–41.
Sillitoe, R.H., Perelló, J., 2005. Andean copper province: tectonomagmatic settings, deposit types, metallogeny, exploration, and discovery. Economic Geology 100th Anniversary Volume, pp. 845–890.
Silva, J.A., Sá, J.A.G., 1986. Jazida de cobre de Chapada, Mara Rosa, Goiás. Principais Depósitos Minerais do Brasil 3 (in Portuguese).
Singer, D.A., Berger, V.I., Moring, B.C., 2008. Porphyry copper deposits of the world: database and grade and tonnage models: U.S. Geological Survey Open-File Report 2008-1155. http://pubs.usgs.gov/of/2008/1155.
Stein, H.J., Hannah, J.L., Zimmerman, A., Markey, R.J., Sarkar, S.C., Pal, A.B., 2004. A 2.5 Ga porphyry Cu–Mo–Au deposit at Malanjkhand, central India: implications for Late Archean continental assembly. Precambrian Res. 134, 189–226.
Strieder, A.J., Suita, M.T.F., 1999. Neoproterozoic tectonic evolution of the Tocantins Structural Province, Central Brazil. J. Geodyn. 28, 267–289.
Thompson, J.F.H., Newberry, R.J., 2000. Gold deposits related to reduced granitic intrusions. Society of Economic Geologists, Reviews 13, pp. 377–400.
Titley, S.R., 1982. The style and progress of mineralization and alteration in porphyry copper systems: American Southwest. In: Titley, S.R. (Ed.), Advances in Geology of the

Porphyry Copper Deposits. University of Arizona Press, southwestern North America: Tucson, pp. 93–116.
Titley, S.R., 1993. Characteristics of porphyry copper occurrence in the American Southwest. Geol. Assoc. Can. Spec. Pap. 40, 433–464.
Tosdal, R.M., Richards, J.P., 2001. Magmatic and structural controls on the development of porphyry Cu ± Mo ± Au deposits. Rev. Econ. Geol. 14, 157–181.
Tosdal, R.M., Dilles, J.H., Cooke, D.R., 2009. From source to sinks in auriferous magmatic–hydrothermal porphyry and epithermal deposits. Elements 5, 289–295.
Valeriano, C.M., Pimentel, M.M., Heilbroni, M., Almeida, J.C.H., Trouw, A.J., 2008. Tectonic evolution of the Brasília Belt, Central Brazil, and early assembly of Gondwana. Geol. Soc. Lond., Spec. Publ. 294, 197–210.
Viana, M.G., Pimentel, M.M., Whitehouse, M.J., Fuck, R.A., Machado, N., 1995. O arco magmático de Mara Rosa, Goiás: dados geoquímicos e geocronológicos e suas implicações regionais. Rev. Bras. Geosci. 25 (2), 111–123 (in Portuguese).
Wilkinson, B.H., Kesler, S.E., 2009. Quantitative identification of metallogenic epochs and provinces: application to Phanerozoic porphyry copper deposits. Econ. Geol. 104, 607–622.
Williams, I.S., Collins, W.J., 1990. Granite–greenstone terranes in the Pilbara Block, Australia, as coeval volcano-plutonic complexes: evidence from U–Pb zircon dating of the Mount Edgar Batholith. Earth Planet. Sci. Lett. 97, 41–53.